

Supplementary Material:

Designing and interpreting 4D tumour spheroid experiments

R. J. Murphy¹, A. P. Browning¹, G. Gunasingh²,
N. K. Haass^{2,†}, and M. J. Simpson^{1,†,*}

¹ *Mathematical Sciences, Queensland University of Technology, Brisbane, Australia*

² *The University of Queensland Diamantina Institute, The University of Queensland, Brisbane,
Australia*

Supplementary Material	Page No.
A. Mathematical model	3
A.1 Nutrient only	3
A.2 Nutrient and waste	8
B. Profile likelihood further details	10
B.1 Numerical method	10
B.2 Parameter bounds	13
B.3 Pooled sample variances	14
C. Experimental data	15
C.1 Outer radius experimental measurements and images	15
C.1.1 Spheroid formation duration	19
C.2 Confocal microscopy	22
C.2.1 Measurements	22
C.3 Confocal microscopy supplementary experimental images	23
C.3.1 WM793b	23
C.3.2 WM983b	27
C.3.3 WM164	30
C.3.4 3D renderings	31
D. Additional results for WM793b	32
D.1 Results in tables	32
D.2 Measurement times and experimental duration	34
D.3 Profile likelihoods for $R_o(0)$	39
D.4 Outer radius measurements are not sufficient to predict inhibited and necrotic radii	40
D.5 Cell cycle data are informative	44
E. Synthetic data based on WM793b	48
E.1 Outer radius measurements are not sufficient to predict inhibited and necrotic radii	48
E.2 Cell cycle data are informative	50
E.3 Role of initial spheroid sizes and experimental duration	51
E.4 Increasing number of measurements	53
F. Parameter identifiability for WM983b	55
F.1 Outer radius measurements are not sufficient to predict inhibited and necrotic radii	56
F.2 Cell cycle data are informative	59
F.3 Information gained across spheroid sizes is consistent	62
G. Parameter identifiability for WM164	63

A Mathematical model

A.1 Nutrient only

Here we recall Greenspan's mathematical model governing the evolution of $R_o(t)$, $R_i(t)$, and $R_n(t)$ (Figure 1f-g). We consider conservation of mass to govern the evolution of $R_o(t)$. Assuming: i) all living cells are identical and an incompressible mass of constant volume; ii) cell division occurs instantaneously relative to the growth time of the tumour, and each daughter cell occupies the same volume as any other cell; iii) the proliferation rate is a constant, s , for cells which have sufficient nutrient; and, iv) the mass density of living cells is constant and equal to density of necrotic debris; then conservation of mass is equivalent to conservation of volume, giving,

$$A = B + C - D - E, \quad (\text{S.1})$$

where A is the total volume of living cells at any time, t ; B is the initial volume of living cells at time $t = 0$; C is the total volume of cells produced in $t \geq 0$; D is the total volume of necrotic debris at time t ; and, E is the total volume lost in the necrotic core in $t \geq 0$.

Writing A, B, C, D, E in their mathematical forms and recalling that the volume and surface area of a sphere with radius r is $4\pi r^3/3$ and $4\pi r^2$, respectively, gives

$$A = \frac{4\pi}{3} (R_o^3(t) - R_n^3(t)), \quad (\text{S.2.1})$$

$$B = \frac{4\pi}{3} R_o^3(0), \quad (\text{S.2.2})$$

$$C = 4\pi \int_0^t \int_{R_i(t)}^{R_o(t)} sr^2 dr dt, \quad (\text{S.2.3})$$

$$D = \frac{4\pi}{3} R_n^3(t), \quad (\text{S.2.4})$$

$$E = \frac{4\pi}{3} \int_0^t 3\lambda R_n^3(t) dt, \quad (\text{S.2.5})$$

where the three inside the integral of equation (S.2.5) is included for mathematical convenience. Substituting equations (S.2.1)-(S.2.5) into equation (S.1) and simplifying gives,

$$R_o^3(t) = R_o^3(0) + 3 \int_0^t \int_{R_i(t)}^{R_o(t)} sr^2 dr dt - \int_0^t 3\lambda R_n^3(t) dt. \quad (\text{S.3})$$

Differentiating equation (S.3) with respect to time and simplifying gives the more useful form,

$$R_o^2(t) \frac{dR_o(t)}{dt} = \underbrace{\frac{s}{3} (R_o^3(t) - R_i^3(t))}_{\text{proliferation of living cells}} - \underbrace{\lambda R_n^3(t)}_{\text{mass lost in necrotic core}}. \quad (\text{S.4})$$

The other important equation concerns the evolution of nutrient within the spheroid. Rewriting

equation (1.2) gives

$$\frac{1}{r^2} \frac{\partial}{\partial r} \left(r^2 \frac{\partial}{\partial r} c(r(t)) \right) = \frac{\alpha}{k} \text{H}(r - R_n(t)) \text{H}(R_o(t) - r), \quad 0 \leq r \leq R_o(t). \quad (\text{S.5})$$

where $\text{H}(\cdot)$ is the Heaviside step function.

To determine the full evolution of the system we solve equations (S.4) and (S.5) together with the nutrient thresholds c_i and c_n which implicitly define $R_i(t)$ and $R_n(t)$, respectively, through

$$c(R_i(t), t) = c_i, \quad (\text{S.6.1})$$

$$c(R_n(t), t) = c_n, \quad (\text{S.6.2})$$

if the nutrient concentration inside the spheroid is sufficiently small otherwise $R_i(t) = 0$ or $R_n(t) = 0$. Note that the equation (S.4) for nutrient does not involve any temporal derivative so the only initial condition required to solve the full system of equations (S.4) and (S.5) is the initial outer radius, $R_o(0)$.

The solution of equation (S.5) is,

$$c(r(t)) = \begin{cases} c_\infty - \frac{\alpha}{6k} (R_o^2(t) - r^2) + \frac{AR_n^3(t)}{3k} \left(\frac{1}{r} - \frac{1}{R_o(t)} \right), & R_n(t) \leq r \leq R_o(t), \\ c_n, & 0 \leq r \leq R_n(t), \end{cases} \quad (\text{S.7})$$

where

$$c_\infty - c_n = \frac{\alpha}{3k} \left[\frac{1}{2} (R_o^2(t) - R_n^2(t)) - \frac{R_n^2(t)}{R_o(t)} (R_o(t) - R_n(t)) \right]. \quad (\text{S.8})$$

The necrotic region first forms when the nutrient concentration reaches c_n at the centre, which occurs when $R_n(t) = 0$ and $r = 0$ in equation (S.8), which gives a critical outer radius,

$$R_c^2 = \frac{6k}{\alpha} (c_\infty - c_n). \quad (\text{S.9})$$

Also recall that $R_i(t)$ corresponds to $c(R_i(t), t) = c_i$ which we can substitute into equation (S.7) to give,

$$c_\infty - c_i = \frac{\alpha}{3k} \left[\frac{1}{2} (R_o^2(t) - R_i^2(t)) - R_n^3(t) \left(\frac{1}{R_i(t)} - \frac{1}{R_o(t)} \right) \right]. \quad (\text{S.10})$$

Since the inhibited region first forms when the nutrient concentration reaches c_i at the centre of the spheroid and the necrotic region forms after the inhibited region, setting $R_n(t) = 0$ and $r = 0$ on right-hand-side of equation (S.10) gives the outer radius when the inhibited region first forms

$$R_d^2 = \frac{6k}{\alpha} (c_\infty - c_i). \quad (\text{S.11})$$

We can then define a useful dimensionless quantity, $Q^2 = R_d^2/R_c^2 = (c_\infty - c_i)/(c_\infty - c_n)$, which is related to the time when phase (ii) begins.

Equations (S.4), (S.5), and (S.6) can now be solved in each of phase (i), (ii), and (iii). To provide valuable insights into the structure of the solutions to the Greenspan model it helps to consider the non-dimensional form of the equations and their solutions. To non-dimensionalise we rescale time with s to give $\tau = st$ and rescale lengths with R_c via $\xi_o(t) = R_o(t)/R_c$, $\xi_i(t) = R_i(t)/R_c$, and $\xi_n(t) = R_n(t)/R_c$. Then phase (ii) starts when $\xi_o(t) = Q$ and phase (iii) starts when $\xi_o(t) = 1$. We now consider each phase in turn.

Phase (i)

In phase (i), all cells are free to proliferate and the nutrient concentration is sufficiently high, i.e. $c(r, t) > c_i$ for $0 \leq r \leq R_o(t)$, such that there is no inhibited or necrotic region (Figure 1(a)). Phase (i) ends when the nutrient concentration at the centre of the spheroid equals the inhibited threshold, when $c(0, t) = c_i$ and $R_o(t) = R_d$.

Since $R_i(t) = 0$ and $R_n(t) = 0$, equation (S.4) becomes

$$R_o^2(t) \frac{dR_o(t)}{dt} = \frac{s}{3} R_o^3(t), \quad (\text{S.12})$$

giving,

$$R_o(t) = R_o(0) \exp\left(\frac{st}{3}\right). \quad (\text{S.13})$$

Non-dimensionalising gives,

$$\xi_o(\tau) = \xi_o(0) \exp\left(\frac{\tau}{3}\right), \quad \text{for } 0 \leq \tau \leq 3 \log\left(\frac{Q}{\xi_o(0)}\right) = \tau_1. \quad (\text{S.14})$$

Given the solution in equation (S.14) we determine $R_o(t)$ by reintroducing s and R_c ,

$$R_o(t) = \xi_o(st)R_c, \quad \text{for } 0 \leq t \leq \frac{\tau_1}{s}. \quad (\text{S.15})$$

Note that $R_i(t) = 0$ and $R_n(t) = 0$ throughout phase (i). Hence, we have obtained $R_o(t)$, $R_i(t)$, $R_n(t)$ throughout this phase.

Phase (ii)

In phase (ii) the spheroid experiences inhibited growth due to a core of inhibited cells and outer region of freely proliferating cells (Figure 1(b)). Phase (ii) ends when the necrotic core forms. Since $R_i(t) > 0$ and $R_n(t) = 0$, equation (S.4) becomes

$$R_o^2(t) \frac{dR_o(t)}{dt} = \frac{s}{3} (R_o^3(t) - R_i^3(t)). \quad (\text{S.16})$$

Non-dimensionalising equation (S.16) gives,

$$\xi_o^2(\tau) \frac{d\xi_o(\tau)}{d\tau} = \frac{1}{3} [\xi_o^3(\tau) - \xi_i^3(\tau)]. \quad (\text{S.17})$$

Equation (S.17) is a function of two variables, $\xi_o(\tau)$ and $\xi_i(\tau)$, which we can simplify to a function of one variable by introducing a change of variables $y_i(\tau) = \xi_i(\tau)/\xi_o(\tau)$, and by using the constraint $Q^2/\xi_o^2(\tau) = 1 - y_i^2(\tau)$, to give

$$\frac{3y_i(\tau)}{(1 - y_i(\tau)^2)(1 - y_i(\tau)^3)} \frac{dy_i(\tau)}{d\tau} = 1, \quad (\text{S.18})$$

with initial condition $y_i(\tau) = 0$ at $\tau = \tau_1$ and terminating condition $y_i(\tau)^2 = 1 - Q^2$. The constraint used to derive equation (S.18) and the termination condition for phase (ii) are obtained with the following argument. In phase (ii) equation (S.10) is

$$R_o^2(t) - R_i^2(t) = R_d^2. \quad (\text{S.19})$$

Non-dimensionalising equations (S.8) and (S.19), using definitions of $\xi_o(\tau)$, $\xi_i(\tau)$, Q , and combining the resulting expressions gives $Q^2 = \xi_o^2(\tau) - \xi_i^2(\tau)$. Rewriting in terms of $y_i(\tau)$ gives $Q^2/\xi_o^2(\tau) = 1 - y_i^2(\tau)$, which gives the constraint used to derive equation (S.18). Using the fact that phase (ii) ends when $\xi_o(\tau) = 1$ and rearranging gives the termination condition for $y_i(\tau)$.

Numerically solving equation (S.18), using MATLAB's in-built *ode15s* differential equation solver [1] with absolute and relative tolerances set to 1×10^{-8} , we obtain $y_i(\tau)$ for phase (ii). To obtain $R_o(t)$ we use the constraint $Q^2/\xi_o^2(\tau) = 1 - y_i(\tau)^2$, and definitions of $\xi_o(\tau)$ and $\xi_i(\tau)$ to obtain $R_o(t) = R_c Q [1 - y_i^2(st)]^{-1/2}$. Similarly using the constraints we obtain $R_i(t) = R_c Q [1/(1 - y_i^2(st)) - 1]^{1/2}$. Recall $R_n(t) = 0$ throughout phase (ii). Hence, we have obtained $R_o(t)$, $R_i(t)$, $R_n(t)$ throughout this phase.

Phase (iii)

In phase (iii) the spheroid experiences inhibited growth due to an outer proliferating region, an inner region of inhibited cells, and a necrotic core (Figure 1(a)). At steady state there is a balance between the number of cells that are proliferating in the outer region and mass lost from the necrotic core.

Since $R_i(t) > 0$ and $R_n(t) > 0$, all terms in equation (S.4) are non-zero. Non-dimensionalising equation (S.4) gives

$$\xi_o^2(\tau) \frac{d\xi_o(\tau)}{d\tau} = \frac{1}{3} [\xi_o^3(\tau) - \xi_i^3(\tau)] - \gamma \xi_n^3(\tau), \quad (\text{S.20})$$

where $\gamma = \lambda/s$. Equation (S.20) is a function of three variables $\xi_o(\tau)$, $\xi_i(\tau)$, $\xi_n(\tau)$. Introducing $y_i(\tau) = \xi_i(\tau)/\xi_o(\tau)$ and $y_n(\tau) = \xi_n(\tau)/\xi_o(\tau)$ we rewrite equation (S.20) and the non-dimensionalised

forms of equations (S.8) and (S.10) as

$$\frac{9y_n(\tau)}{(1+2y_n(\tau))(1-y_n(\tau))} \frac{dy_n(\tau)}{d\tau} = 1 - y_i^3(\tau) - 3\gamma y_n^3(\tau), \quad (\text{S.21.1})$$

$$\xi_o^{-2}(\tau) = (1 - y_n(\tau))^2 (1 + 2y_n(\tau)), \quad (\text{S.21.2})$$

$$\frac{Q^2}{\xi_o^2(\tau)} = 1 - y_i^2(\tau) - 2y_n^3(\tau) \left(\frac{1 - y_i(\tau)}{y_i(\tau)} \right), \quad (\text{S.21.3})$$

noting that equation (S.21.1) is obtained using equation (S.21.2). Then we numerically solve equations (S.21.1)-(S.21.3) to obtain $y_i(\tau)$ and $y_n(\tau)$ using the the following approach. First, we substitute equation (S.21.2) into equation (S.21.3) to eliminate $\xi_o(\tau)$ and rearrange which gives

$$0 = -Q^2 \left[(1 - y_n(\tau))^2 (1 + 2y_n(\tau)) \right] + 1 - y_i^2(\tau) - 2y_n^3(\tau) \left(\frac{1 - y_i(\tau)}{y_i(\tau)} \right). \quad (\text{S.22})$$

Equations (S.21.1) and (S.22) form a system of differential-algebraic equations which we numerically solve using MATLAB's in-built *ode15s* solver with relative and absolute tolerances set to 1×10^{-8} . Given the solution for $y_n(\tau)$ and $y_i(\tau)$ we obtain $R_o(t)$, $R_i(t)$ and $R_n(t)$ using the following approach. Given $y_n(\tau)$ we obtain $\xi_o(\tau)$ using equation (S.21.2). Then $R_o(t) = R_c \xi_o(st)$. Using the definition of $y_i(\tau)$, $y_n(\tau)$ and $\xi_o(\tau)$ we obtain $R_i(t) = R_c y_i(st) \xi_o(st)$ and $R_n(t) = R_c y_n(st) \xi_o(st)$. Hence, we have obtained $R_o(t)$, $R_i(t)$, $R_n(t)$ throughout this phase. Key software for this section is freely available on a GitHub repository.

The approach taken in phases (i), (ii), and (iii) means that we do not require knowledge of the values of the parameters c_∞ , c_n , c_i , k and α but instead only the value of $Q = [(c_\infty - c_i)/(c_\infty - c_n)]^{1/2}$. This reduces the number of parameters describing the evolution of the spheroid from eight to five. The three pieces of information no longer consider regard the nutrient concentration which we do not directly measure in this study and has been explored in other studies [2,3]. Furthermore, equations (S.8)-(S.10) show that there are constraints on the relationships between $R_o(t)$, $R_i(t)$, $R_n(t)$ which can be explored further.

A.2 Nutrient and waste

The model presented in methods section 4.1 and supplementary material A.1 is a special case of Greenspan's model [4]. The general Greenspan model proposes the inhibited region is a result of a build up of waste produced from live or dead cells and the necrotic region forms due to a lack of nutrient. Here, we consider the alternative case where waste is produced from live cells only and show that, for the measurements we obtain, it is equivalent to the nutrient only case we consider in the main manuscript (Figure S1). We do not consider waste produced only from dead cells in this study since with that model the necrotic core must form before the inhibited region which is not what we observe in these experiments (Figure 1(b)).

In comparison to the nutrient only model in supplementary material A.1, the model with nutrient and waste requires an additional equation for the evolution of waste concentration, $\beta(r, t)$. The full system of governing equations are,

$$R_o^2(t) \frac{dR_o(t)}{dt} = \frac{s}{3} [R_o^3(t) - \max(R_n^3(t), R_i^3(t))] - \lambda R_n^3(t), \quad (\text{S.23.1})$$

$$\frac{1}{r^2} \frac{\partial}{\partial r} \left(r^2 \frac{\partial}{\partial r} c(r(t)) \right) = \frac{\alpha}{k} H(r - R_n(t)) H(R_o(t) - r), \quad 0 \leq r \leq R_o(t), \quad (\text{S.23.2})$$

$$\frac{1}{r^2} \frac{\partial}{\partial r} \left(r^2 \frac{\partial}{\partial r} \beta(r(t)) \right) = \frac{P}{\kappa} H(R_n(t) - r), \quad 0 \leq r \leq R_o(t), \quad (\text{S.23.3})$$

where equations (S.23.1) and (S.23.2) are unchanged, by restricting our attention to the case when the inhibited region forms before the necrotic region, and equation (S.23.3) is new. In equation (S.23.3), the term on the right-hand-side corresponds to production of waste by live cells at a constant rate per unit volume P that diffuses with diffusivity κ . Furthermore, $R_i(t)$ is defined as the solution of $\beta(R_i(t), t) = \beta_i$ if a solution exists and $R_i = 0$ otherwise.

This model, with nutrient and waste, is equivalent to the nutrient only model when we focus on the five key parameters $R_o(0), R_c, s, \gamma, Q$ governing the dynamics. The only difference is a new definition of Q ,

$$Q^2 = \underbrace{\frac{\beta_i \kappa}{P}}_{\text{waste parameters}} \underbrace{\frac{\alpha}{k(c_\infty - c_n)}}_{\text{oxygen parameters}}. \quad (\text{S.24})$$

This new definition of Q provides a different interpretation of the data since Q now represents a combination of waste and nutrient parameters. Importantly, with this new definition of Q there are two cases to consider: i) $Q \leq 1$, and ii) $Q > 1$. Previously, we only considered case (i). In case (ii) where $Q > 1$ the necrotic core forms before the inhibited region. We do not observe this scenario in the experiments that we perform and therefore we restrict the attention of this study to case (i) with $Q \leq 1$.

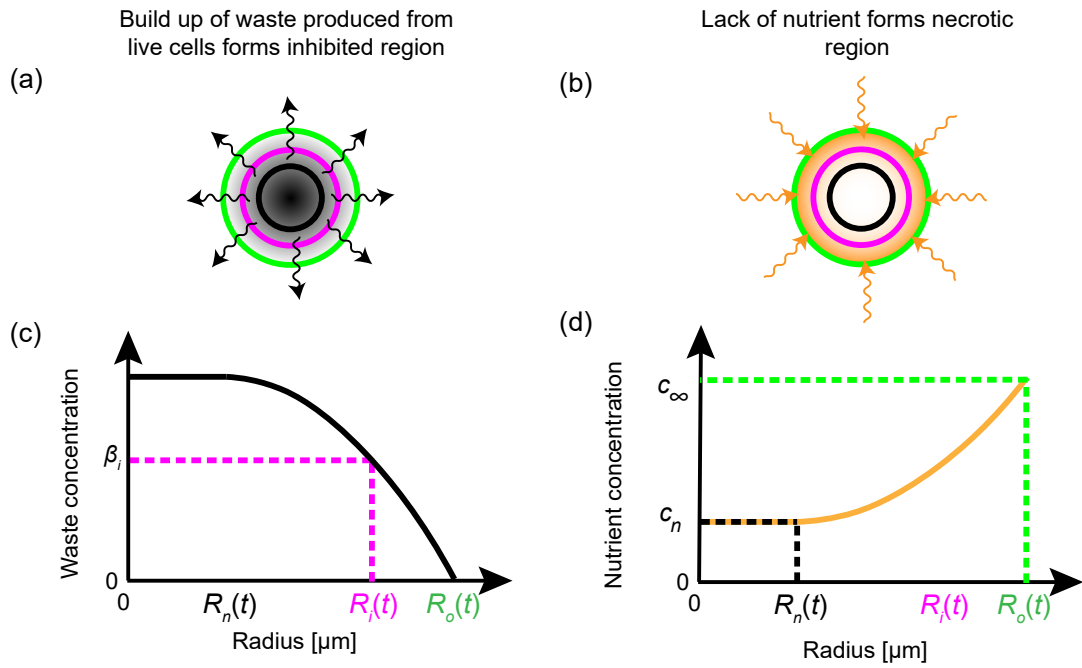


Figure S1: Greenspan's model with waste and nutrient. (a),(c) Build up of waste from live cells results in the formation of an inhibited region. (a) Schematic of waste produced from live cells and diffusing to the external environment. (c) Snapshot of waste concentration against spheroid radius for a spheroid in phase (iii). $R_i(t)$ is determined by the inhibited waste threshold β_i . (b),(d) Lack of nutrient forms the necrotic region. (b) Nutrient, shown in orange, diffusing into the spheroid. (d) Snapshot of nutrient concentration against spheroid radius for a spheroid in phase (iii). $R_n(t)$ is determined by the necrotic nutrient threshold c_n . External nutrient concentration is c_∞ .

B Profile likelihood further details

B.1 Numerical method

Parameter identifiability using statistical profile likelihood analysis is outlined in the methods section 4.2. We now provide further details.

We partition the full set of observations y^o into sets of observations y_o^o , y_n^o , and y_i^o corresponding to experimental measurements of $R_o(t)$, $R_n(t)$, and $R_i(t)$. For computational accuracy, we perform calculations using the log-likelihood which is, assuming data independence,

$$l(\theta; y^o) = \sum_{j=1}^{N_o} \log [f(y_{o,j}^o; y_{o,j}(\theta), \sigma_o^2)] + \sum_{j=1}^{N_n} \log [f(y_{n,j}^o; y_{n,j}(\theta), \sigma_n^2)] + \sum_{j=1}^{N_i} \log [f(y_{i,j}^o; y_{i,j}(\theta), \sigma_i^2)], \quad (\text{S.25})$$

where $y_{o,j}(\theta)$, $y_{n,j}(\theta)$, and $y_{i,j}(\theta)$ are values of $R_o(t)$, $R_n(t)$, and $R_i(t)$ generated from the deterministic Greenspan model and evaluated at time points corresponding to the experimental observations $y_{o,j}^o$, $y_{n,j}^o$, and $y_{i,j}^o$, respectively; $f(x; \mu, \sigma^2)$ denotes a Gaussian probability density function with mean μ and variance σ^2 , calculated using MATLAB's `normpdf` function [5]; N_o , N_n , and N_i denote the total number of experimental observations of $R_o(t)$, $R_n(t)$, and $R_i(t)$, respectively; and, σ_o^2 , σ_n^2 , and σ_i^2 correspond to pooled variances of the three measurement types $R_o(t)$, $R_n(t)$, and $R_i(t)$, respectively [6, 7]. We approximate $\sigma_o^2 \approx s_o^2$, $\sigma_n^2 \approx s_n^2$, and $\sigma_i^2 \approx s_i^2$, where s_o^2 , s_n^2 , s_i^2 are pooled sample variances of the outer, necrotic, and inhibited radius measurements, respectively [8]. The pooled sample variance for the outer radius is defined as

$$s_o^2 = \frac{1}{N_o - 1} \sum_{j=1}^{N_o} (y_{o,j}^o - \overline{y_{o,j}^o})^2, \quad (\text{S.26})$$

where $y_{o,j}^o$ is the j^{th} observation in y_o^o and $\overline{y_{o,j}^o}$ is the sample mean of y_o^o corresponding to the time at which the j^{th} measurement was observed. We define s_n^2 and s_i^2 similarly.

The maximum likelihood estimate (MLE), $\hat{\theta}$, is defined as,

$$\hat{\theta} = \operatorname{argmax}_{\theta} [l(\theta; y^o)], \quad (\text{S.27})$$

which we determine by numerically solving the equivalent minimisation problem,

$$\hat{\theta} = \operatorname{argmin}_{\theta} [-l(\theta; y^o)]. \quad (\text{S.28})$$

By assuming the full parameter θ can be partitioned into an interest scalar parameter, ψ , and a

nuisance vector parameter, ϕ , the profile log-likelihood is

$$l_p(\psi; y^0) = \max_{\phi} \left[\sum_{j=1}^{N_o} \log [f(y_{o,j}^o; y_{o,j}(\psi, \phi), \sigma_o^2)] + \sum_{j=1}^{N_n} \log [f(y_{n,j}^o; y_{n,j}(\psi, \phi), \sigma_n^2)] \right. \\ \left. + \sum_{j=1}^{N_i} \log [f(y_{i,j}^o; y_{i,j}(\psi, \phi), \sigma_i^2)] \right]. \quad (\text{S.29})$$

Given the five-dimensional parameters space that we are searching to find the maximum likelihood estimate and the four-dimensional parameter space we search to find profile likelihoods, we sequentially determine the maximum likelihood estimate (MLE) and profile likelihoods. All subsequent minimisation optimisations are performed using functions in MATLABs global optimisation toolbox. Specifically, we use the *GlobalSearch* function [9] where we create the following optimisation problem structure. We set the local solver to be the *fmincon* function using the sequential quadratic programming (sqp) algorithm, **MaxIterations** = 2500 and **MaxFunctionEvaluations** = 5000. The objective function is defined as the argument of the minimisation of the right hand side of equation (S.28). Other non-default settings that we vary, include **NumTrialPoints**, **MaxTime**, **FirstGuess**, **lowerbounds**, **upperbounds**, along with the method we use to find the MLE and approximate 95% confidence intervals are now discussed.

1. Firstly, we search for MLE. We set the **lowerbounds** and **upperbounds** in agreement with the simple parameter bounds defined in the methods section 4.2. By setting **NumTrialPoints** = 5000 and **MaxTime** = 7200 [seconds], we search for the maximum likelihood estimate for 2 hours with the **FirstGuess** as $(Q, \gamma, s, R_c, R_o(0)) = (0.9, 3, 0.5, 175, 125)$. This gives the first estimate for the maximum likelihood estimate $\hat{\theta}_1$. However, numerical experimentation indicates this first estimate is not always an accurate estimate of the true MLE.
2. Secondly, we partition the simple parameter bounds into two sets: [**lowerbounds**, $\hat{\theta}_1$] which we refer to as the lower set, and [$\hat{\theta}_1$, **upperbounds**] which we refer to as the upper set. We then discretise each lower and upper set uniformly using 20 grid points, including the end points. Starting at the grid point associated with $\hat{\theta}_1$ we set **FirstGuess** = $\hat{\theta}_1$, **NumTrialPoints** = 2000 and **MaxTime** = 900 [seconds] in the *GlobalSearch* function. We then move to the next closest grid point and adjust **FirstGuess**. If we are at the closest grid point to $\hat{\theta}_1$ we set **FirstGuess** to be the solution at the previous gridpoint. If we are at any other grid point we make a first order approximation of the first guess by linear extrapolation of the values obtained from the two previous grid points. Before using the first order approximation as a first guess we also check that the value remains within the parameter bounds and if it does not we set **FirstGuess** to be the solution at the previous gridpoint. After calculating the likelihood at each point in the lower and upper set we combine these together to form the first approximation for the profile likelihood.
3. Thirdly, we estimate confidence intervals thresholds using a profile likelihood threshold value of

0.15, which can be approximately calibrated via simulation or the χ^2 -distribution [10]. Specifically, we start at either end of the simple parameter bounds until we determine the first grid point where the normalised profile likelihood, $L_p(\psi; y^0) = \exp\left(l_p(\psi; y^0) - \max_{\theta} [l(\theta; y^0)]\right)$, is greater than 0.15. We then set new lower and upper bounds as being two grid points to the left or right of that location, respectively.

4. Fourth, we repeat the search for the maximum likelihood estimate using the new lower and upper bounds with the same settings as we first used.
5. Fifth, we repeat the calculations for the profile likelihoods using the new lower and upper bounds.
6. Finally, we determine the maximum likelihood estimate to be the value across all calculations which maximises the likelihood. We form the final profile likelihood from steps two and four and present the normalised likelihood function, $L_p(\psi; y^0) = \exp\left(l_p(\psi; y^0) - \max_{\theta} [l(\theta; y^0)]\right)$, in figures.

B.2 Parameter bounds

To interpret s we consider the evolution of the tumour spheroid in phase (i). Equation (S.13) can be written in terms of volume $V(t)$, recalling that the volume of a sphere is $4\pi R_o^3(t)/3$, as

$$V(t) = V(0) \exp(st), \tag{S.30}$$

where $V(0) = 4\pi R_o^3(0)/3$. Then by letting T define the time when $V(T) = 2V(0)$, we relate s to the doubling time of the cells through

$$s = \frac{1}{T} \log_e(2). \tag{S.31}$$

Then assuming that the doubling time is greater than 12 hours ($= 1/2$ day) we obtain an upper bound of s as $2 \log_e(2)$ [day^{-1}] ≈ 1.39 [day^{-1}]. Preliminary exploration confirms this estimate is very conservative so we set the upper bound to unity.

B.3 Pooled sample variances

To identify parameters we assume distinct pooled sample variances for the outer, necrotic, and inhibited radius measurements, as opposed to a single pooled variance for all measurements. In Figure S2 we plot the pooled sample variances for different experimental designs which justify the use of a variance for each measurement type.

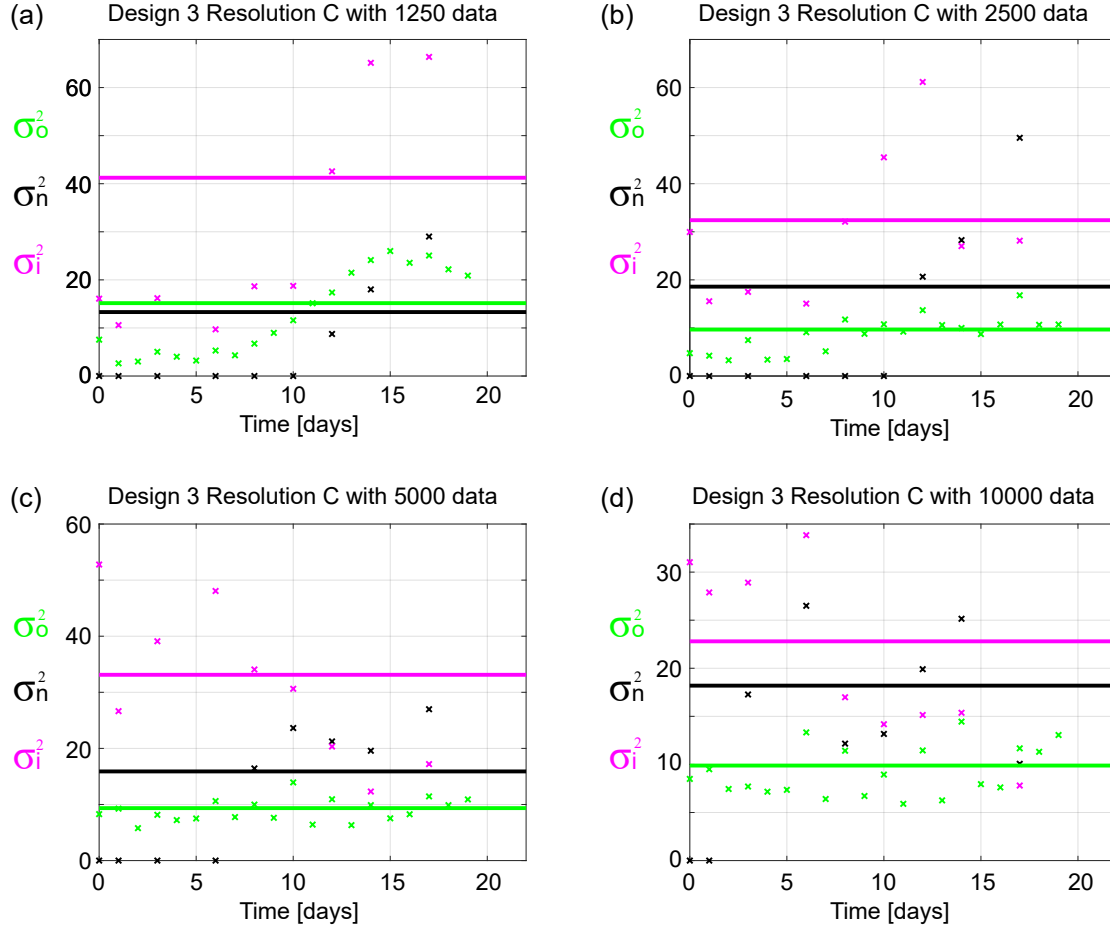


Figure S2: Variances σ_o^2 , σ_n^2 , and σ_i^2 , for outer, necrotic and inhibited radii, respectively. Results shown for WM793b spheroids, using Design 3 and Temporal Resolution C, formed with (a) 1250, (b) 2500, (c) 5000, (d) 10000 cells per spheroid, respectively.

C Experimental data

C.1 Outer radius experimental measurements and images

The IncuCyte S3 live cell imaging system is a useful tool that we use to obtain many outer radius measurements. The other outer radius measurements are obtained from confocal microscopy.

We start with 24 spheroids in the IncuCyte S3 live cell imaging system for each cell line and initial spheroid size and image every 6 hours for the duration of the experiment. However, some measurements could not be obtained primarily due to blurring of the automated imaging, spheroids not forming properly, or spheroids losing their structural integrity at very late time. In Table S1 we show the total number of measurements obtained at 24 hour intervals starting from Day 0 which corresponds to the time that we determined as when spheroid formation ends and growth begins (Supplementary Material C.1.1). In Figures S3-S5 we present representative experimental images obtained from IncuCyte S3 live cell imaging system for different days and WM793b, WM983b, and WM164 cell lines, respectively.

Day	WM793				WM983b			WM164			
	1250	2500	5000	10000	2500	5000	10000	1250	2500	5000	10000
0	20	24	24	23	24	22	23	23	22	23	21
1	20	23	24	23	24	22	23	24	22	24	21
2	20	23	24	23	24	22	23	18	22	24	20
3	21	23	24	23	24	22	23	19	23	24	20
4	21	24	24	23	24	22	23	18	23	24	20
5	21	23	24	23	24	22	22	19	20	19	-
6	21	24	24	23	24	22	21	19	19	19	-
7	21	24	24	23	23	22	20	-	-	-	-
8	21	24	24	23	23	22	20	-	-	-	-
9	21	24	24	23	23	22	20	-	-	-	-
10	21	24	24	23	23	22	20	-	-	-	-
11	21	24	24	23	23	22	20	-	-	-	-
12	21	24	24	23	22	22	20	-	-	-	-
13	21	24	24	23	22	22	20	-	-	-	-
14	21	24	24	23	-	-	-	-	-	-	-
15	20	24	22	23	22	22	20	-	-	-	-
16	18	24	22	23	22	22	20	-	-	-	-
17	18	24	22	23	22	22	20	-	-	-	-
18	19	24	22	23	22	22	20	-	-	-	-
19	19	24	22	23	22	22	20	-	-	-	-
20	13	24	13	11	-	-	-	-	-	-	-

Table S1: Number of outer radius measurements obtained from the IncuCyte S3 live cell imaging system for the cell lines WM793b, WM983b, and WM164. Day 0 corresponds to the time that we determined as when spheroid formation ends and growth begins, see supplementary material C.1.1.

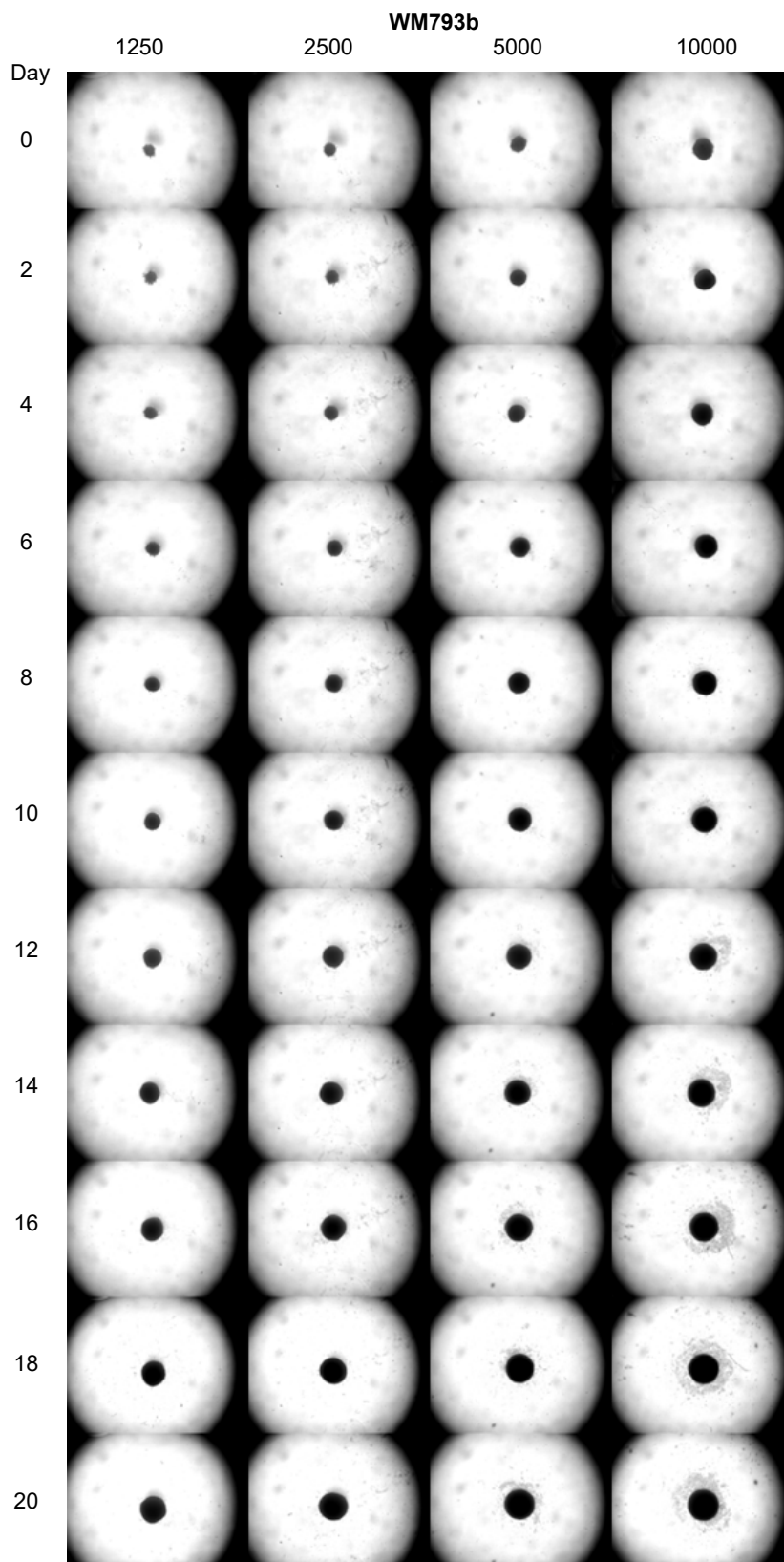


Figure S3: Snapshots of WM793b tumour spheroids from IncuCyte S3 live cell imaging system at 0, 2, 4, 6, 8, 10, 12, 14, 16, 18, and 20 days after formation for tumour spheroids formed with 1250, 2500, 5000, and 10000 cells per spheroid. Each image shows a 4.34×3.25 mm field of view.

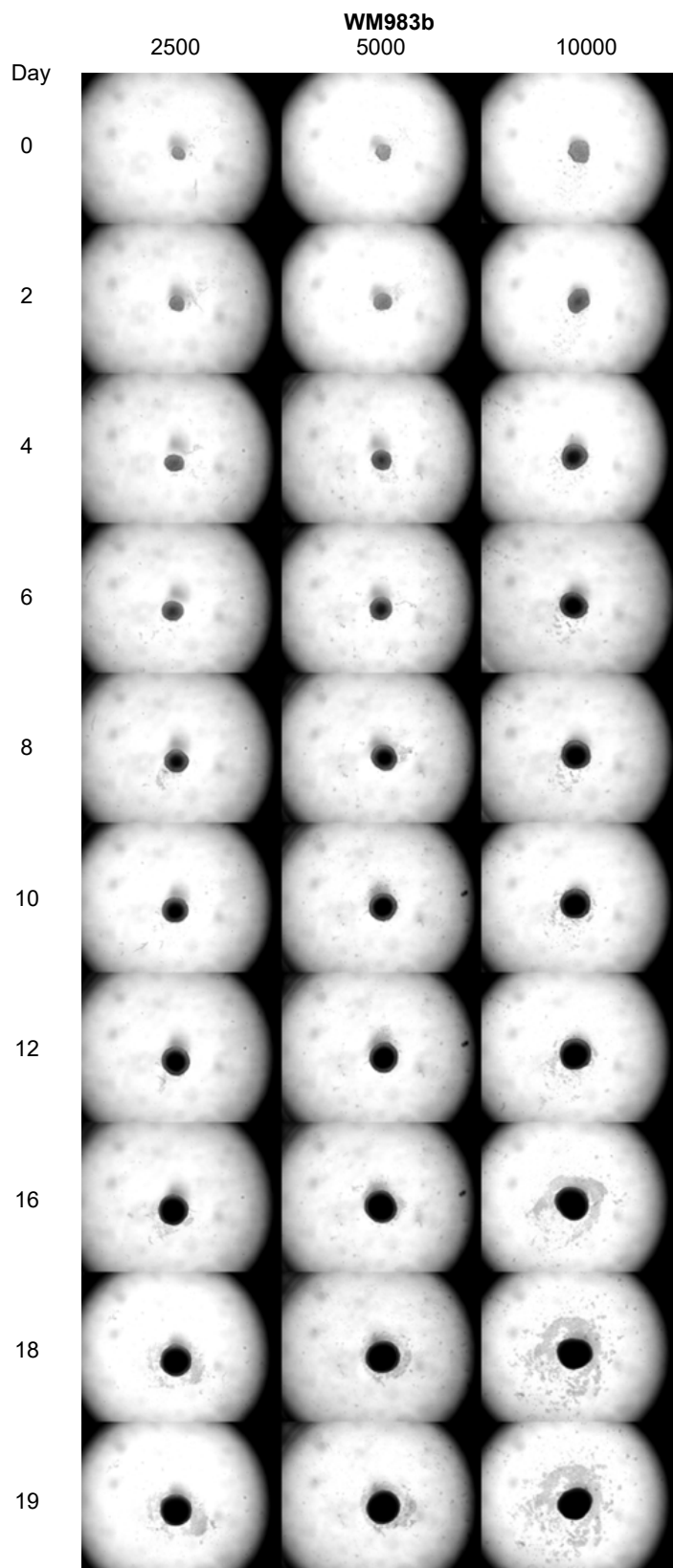


Figure S4: Snapshots of WM983b tumour spheroids from IncuCyte S3 live cell imaging system at 0, 2, 4, 6, 8, 10, 12, 16, 18, and 19 days after formation for tumour spheroids formed with 2500, 5000, and 10000 cells per spheroid. Each image shows a 4.34×3.25 mm field of view.

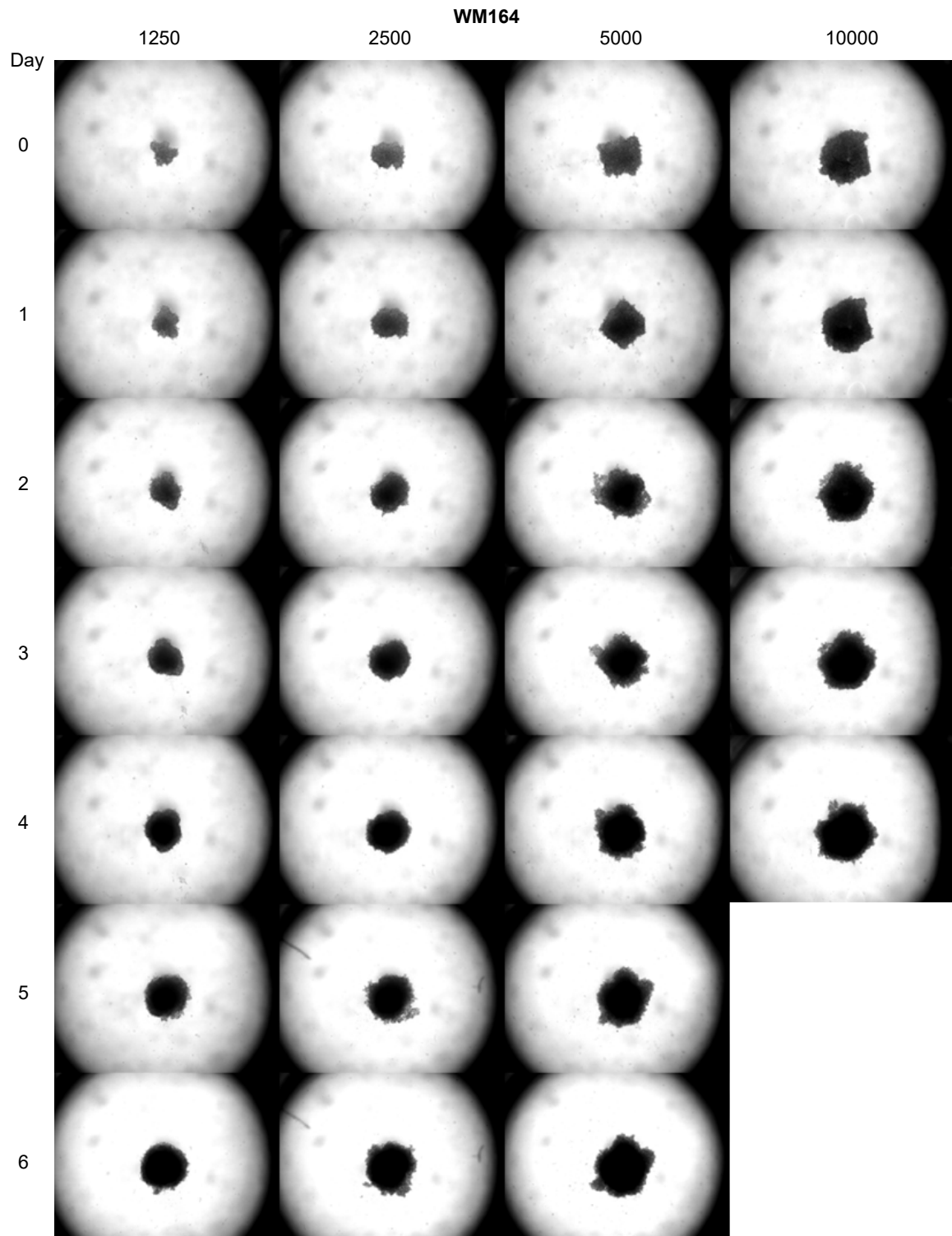


Figure S5: Snapshots of WM164 tumour spheroids from IncuCyte S3 live cell imaging system at 0, 1, 2, 3, 4, 5, and 6 days after formation for tumour spheroids formed with 1250, 2500, 5000, and 10000 cells per spheroid. Each image shows a 4.34×3.25 mm field of view.

C.1.1 Spheroid formation duration

In Figure S6 we show time snapshots of forming tumour spheroids obtained in the IncuCyte S3 live cell imaging system. These snapshots, alongside monitoring the evolution of the outer radius obtained from image processing, validate the assumption that the tumour spheroids have formed 4 days after seeding for WM793b. This method was also used to determine the duration of spheroid formation for the WM983b (Figure S7) and WM164 (Figure S8) cell lines.

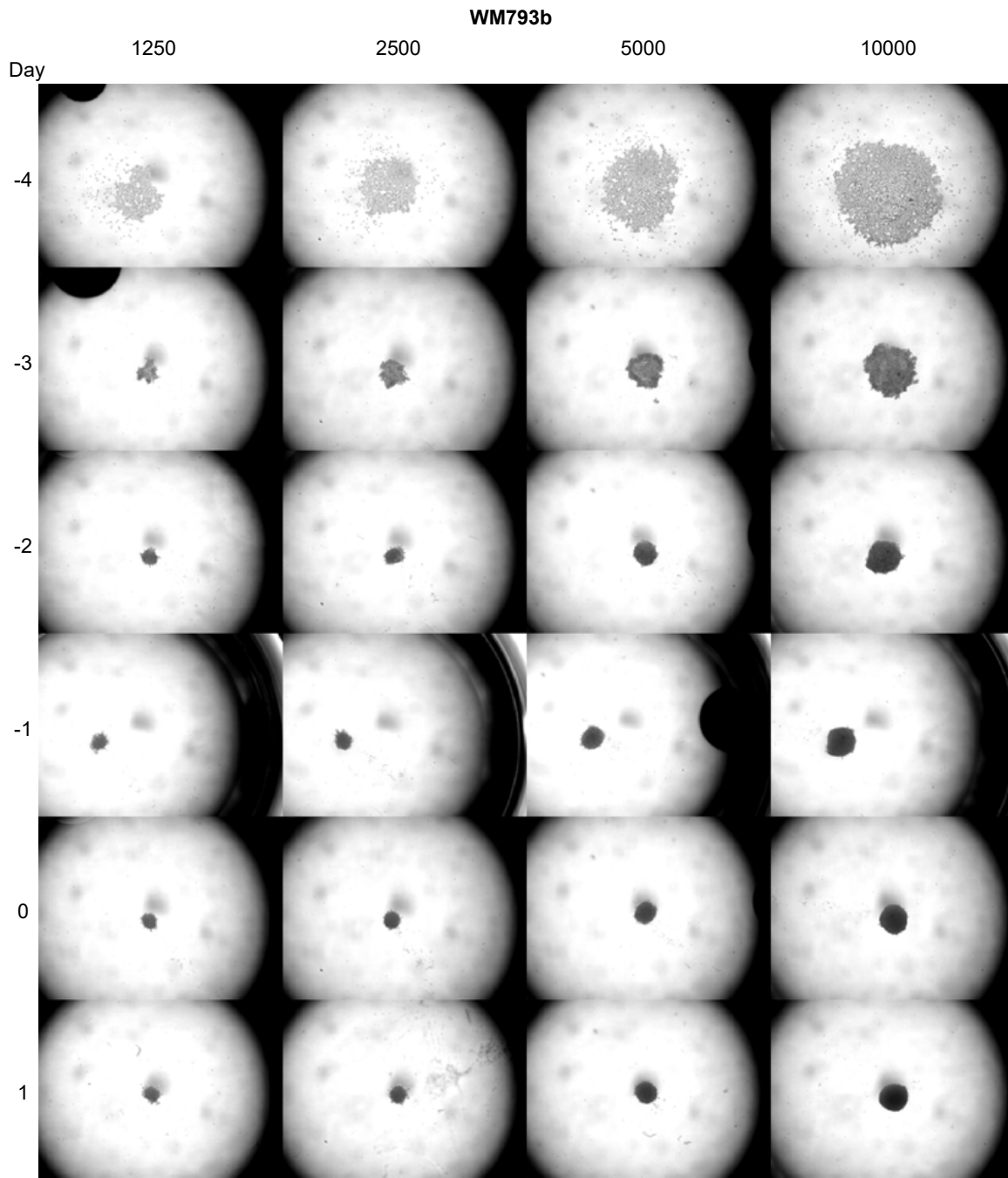


Figure S6: Spheroids are formed 4 days after seeding for WM793b. Snapshots from IncuCyte S3 live cell imaging system at -4, -3, -2, -1, 0, and 1 days after formation for tumour spheroids formed 1250, 2500, 5000, and 10000 cells per spheroid. Each image shows a 4.34×3.25 mm field of view.

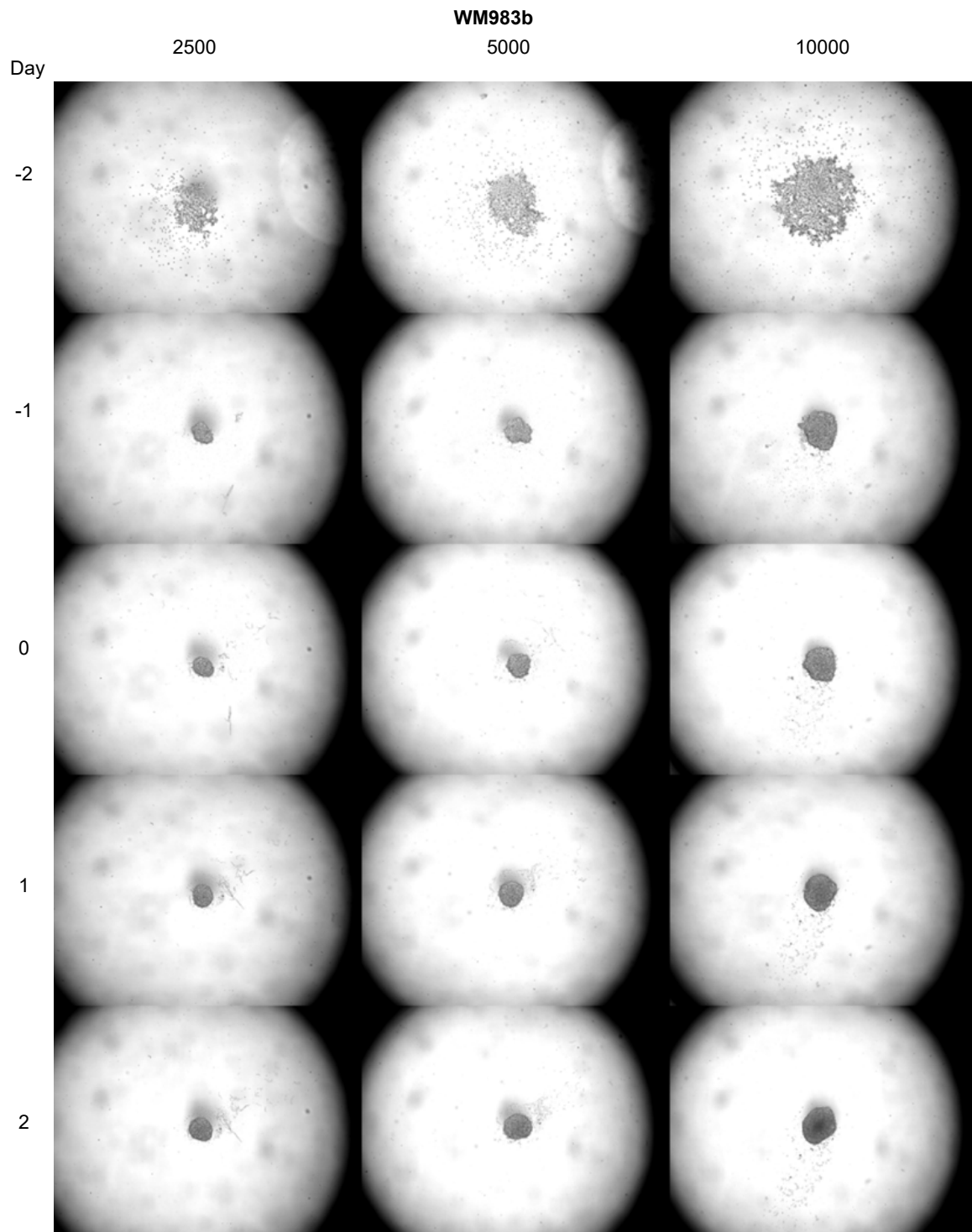


Figure S7: Spheroids are formed at 2 days after seeding for WM983b. Snapshots from IncuCyte S3 live cell imaging system at -2, -1, 0, 1, and 2 days after formation for tumour spheroids formed with 2500, 5000, and 10000 cells per spheroid. Each image shows a 4.34×3.25 mm field of view.

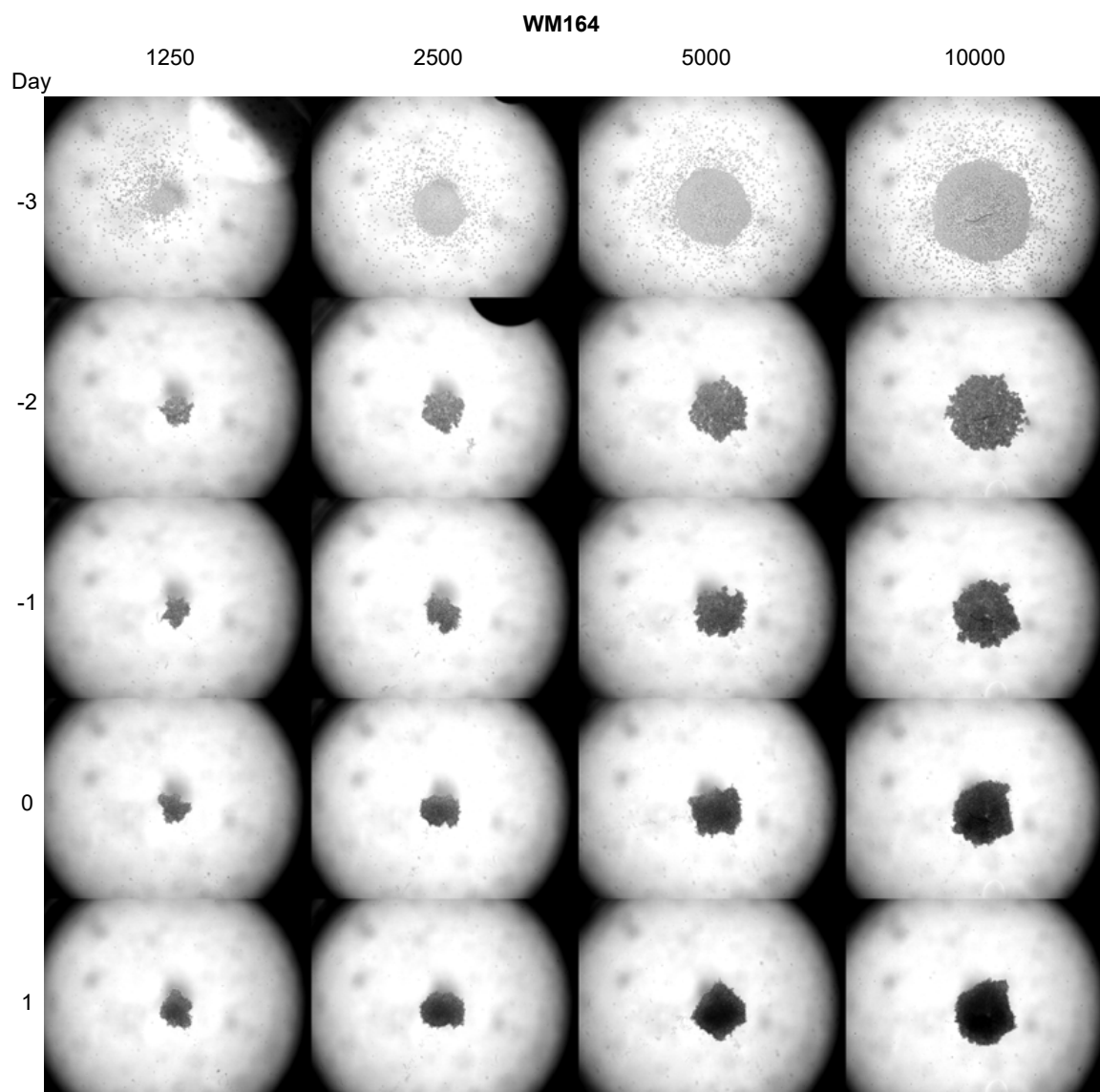


Figure S8: Spheroids are formed at 3 days after seeding for WM164. Snapshots from IncuCyte S3 live cell imaging system at -3, -2, -1, 0 and 1 days after formation for tumour spheroids formed with 1250, 2500, 5000, and 10000 cells per spheroid. Each image shows a 4.34×3.25 mm field of view.

C.2 Confocal microscopy

C.2.1 Measurements

In Table S2 we show the number of confocal measurements obtained. Spheroids damaged during harvesting and fixing procedures are not included.

Day	WM793				WM983b			WM164			
	1250	2500	5000	10000	2500	5000	10000	1250	2500	5000	10000
0	5	5	12	7	-	-	-	-	-	-	-
1	4	10	11	12	6	9	6	6	4	14	6
2	-	-	-	-	12	9	10	13	10	10	9
3	5	22	23	18	12	10	9	-	-	-	-
4	-	-	-	-	-	-	-	13	8	-	-
5	-	-	-	-	20	15	18	-	-	-	-
6	7	28	25	25	-	-	-	-	-	-	-
7	-	-	-	-	-	-	-	-	-	-	-
8	12	27	20	23	16	13	15	-	-	-	-
9	-	-	-	-	-	-	-	-	-	-	-
10	8	19	21	15	16	17	21	-	-	-	-
11	-	-	-	-	-	-	-	-	-	-	-
12	12	18	19	17	13	14	13	-	-	-	-
13	-	-	-	-	-	-	-	-	-	-	-
14	15	19	22	21	17	21	19	-	-	-	-
15	-	-	-	-	-	-	-	-	-	-	-
16	-	-	-	-	11	20	19	-	-	-	-
17	11	15	14	5	-	-	-	-	-	-	-
18	-	-	-	-	-	-	-	-	-	-	-
19	-	-	-	-	25	31	16	-	-	-	-
20	22	23	21	20	-	-	-	-	-	-	-

Table S2: Number of spheroids imaged using confocal microscopy for the cell lines WM793b, WM983b, and WM164. For each imaged spheroid we obtain a measurement of the outer radius, inhibited radius, and necrotic radius. Day 0 corresponds to the time for the each cell line that we determined as when spheroid formation ends and growth begins. Measurements were taken on days 3, 4, 5, 7, 10, 12, 14, 16, 18, 21 and 24 after seeding, and appear on different days in the table due to the different formation times.

C.3 Confocal microscopy supplementary experimental images

Here we present confocal microscopy images of spheroids formed with the WM793b, WM983b, and WM164 cell lines. In the images we outline each spheroids outer boundary, inhibited region, and necrotic region.

C.3.1 WM793b

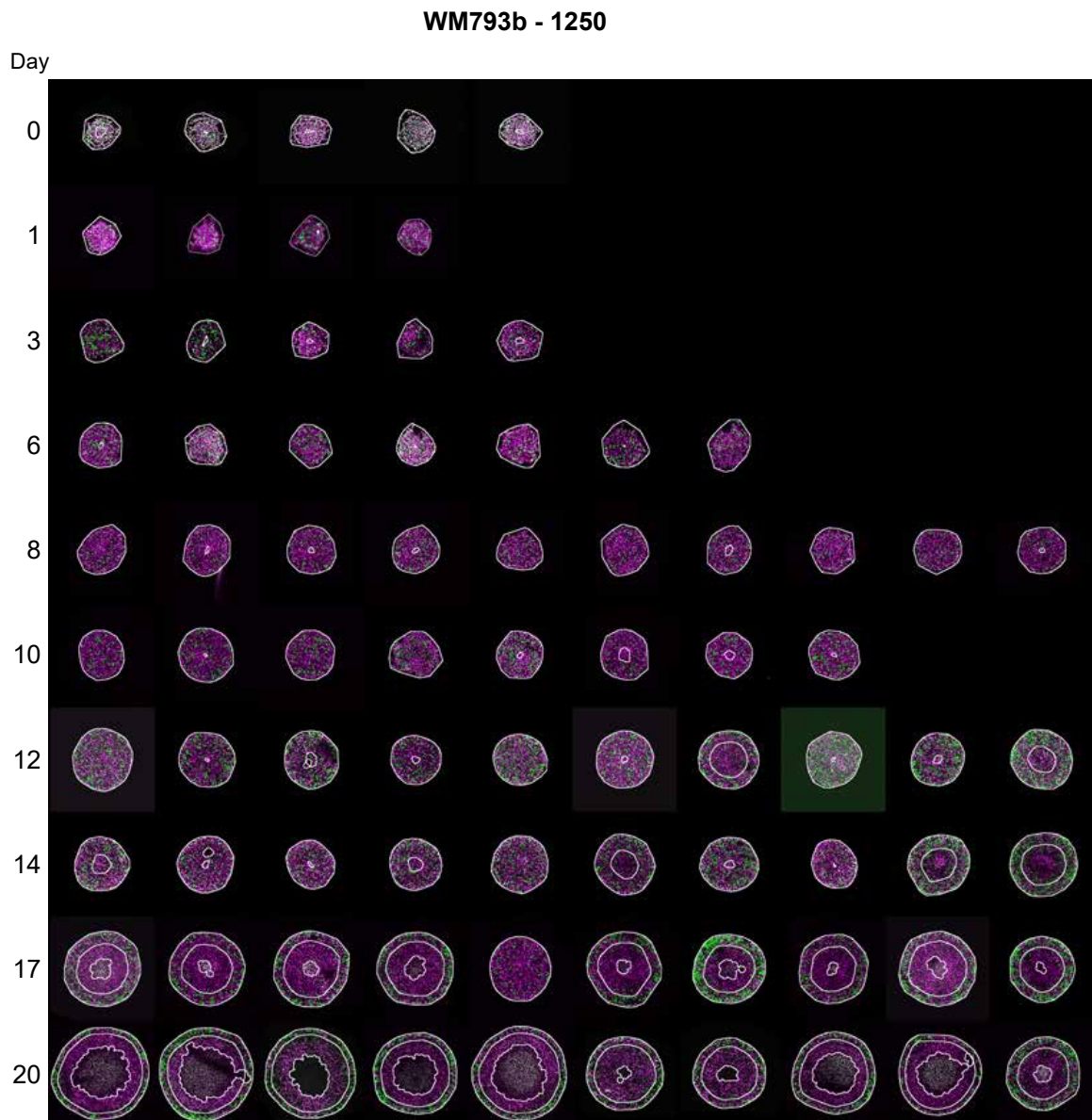


Figure S9: Experimental images of WM793b tumour spheroids formed with 1250 cells per spheroid. Each image shows a $800 \times 800 \mu\text{m}$ field of view.

WM793b - 2500

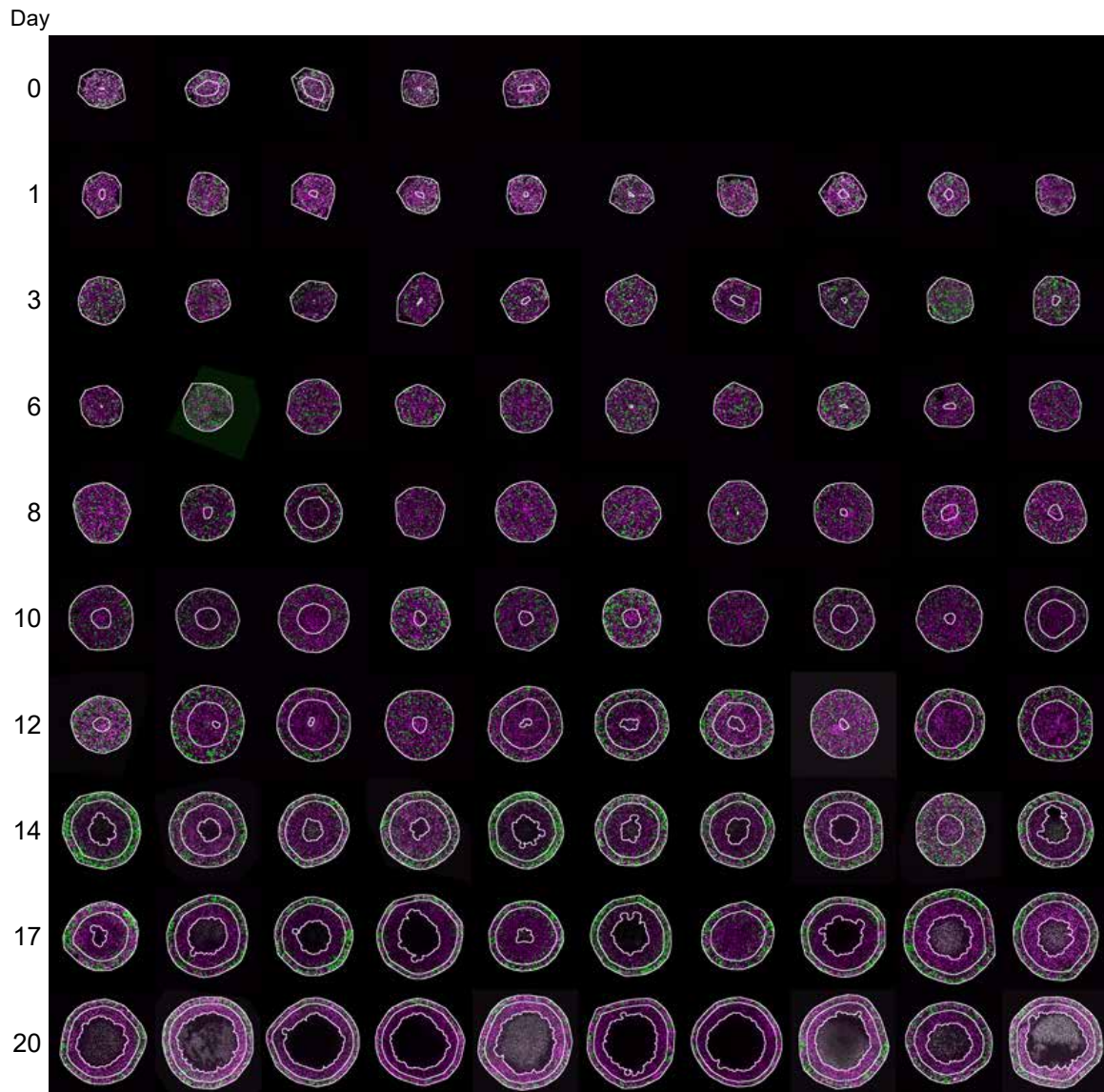


Figure S10: Experimental images of WM793b tumour spheroids formed with 2500 cells per spheroid. Each image shows a $800 \times 800 \mu\text{m}$ field of view.

WM793b - 5000

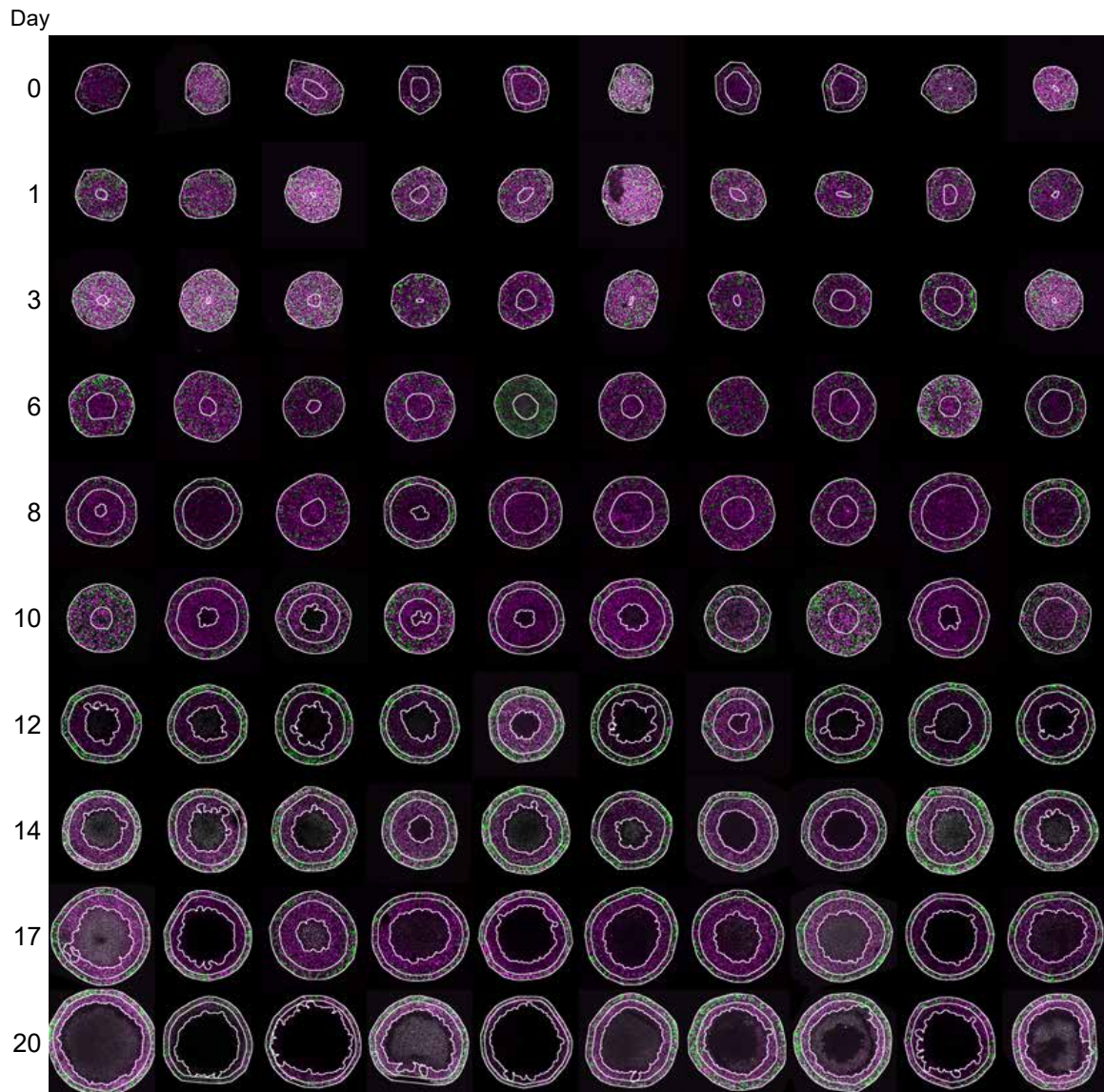


Figure S11: Experimental images of WM793b tumour spheroids formed with 5000 cells per spheroid. Each image shows a $800 \times 800 \mu\text{m}$ field of view.

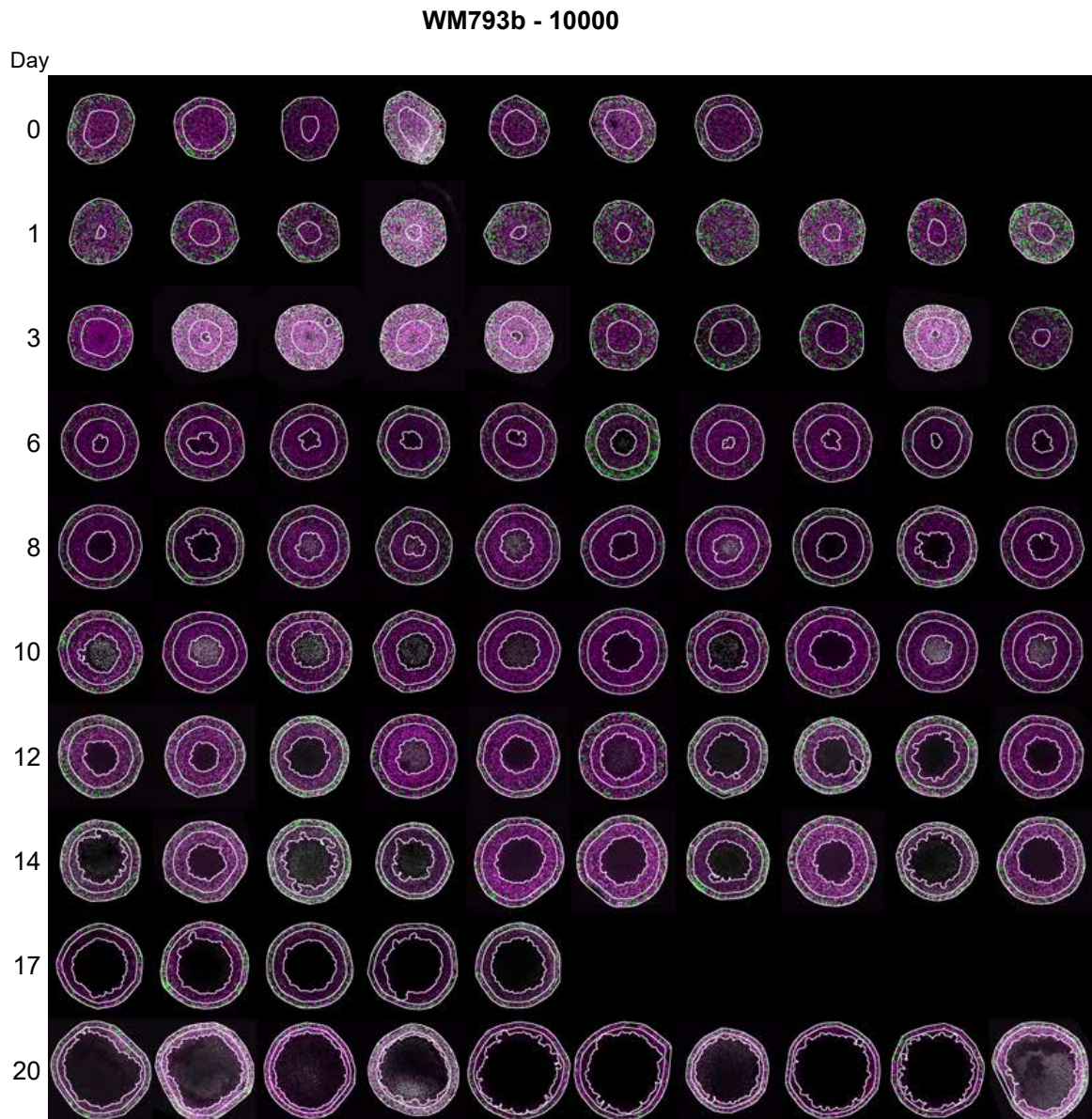


Figure S12: Experimental images of WM793b tumour spheroids formed with 10000 cells per spheroid. Each image shows a $800 \times 800 \mu\text{m}$ field of view.

C.3.2 WM983b

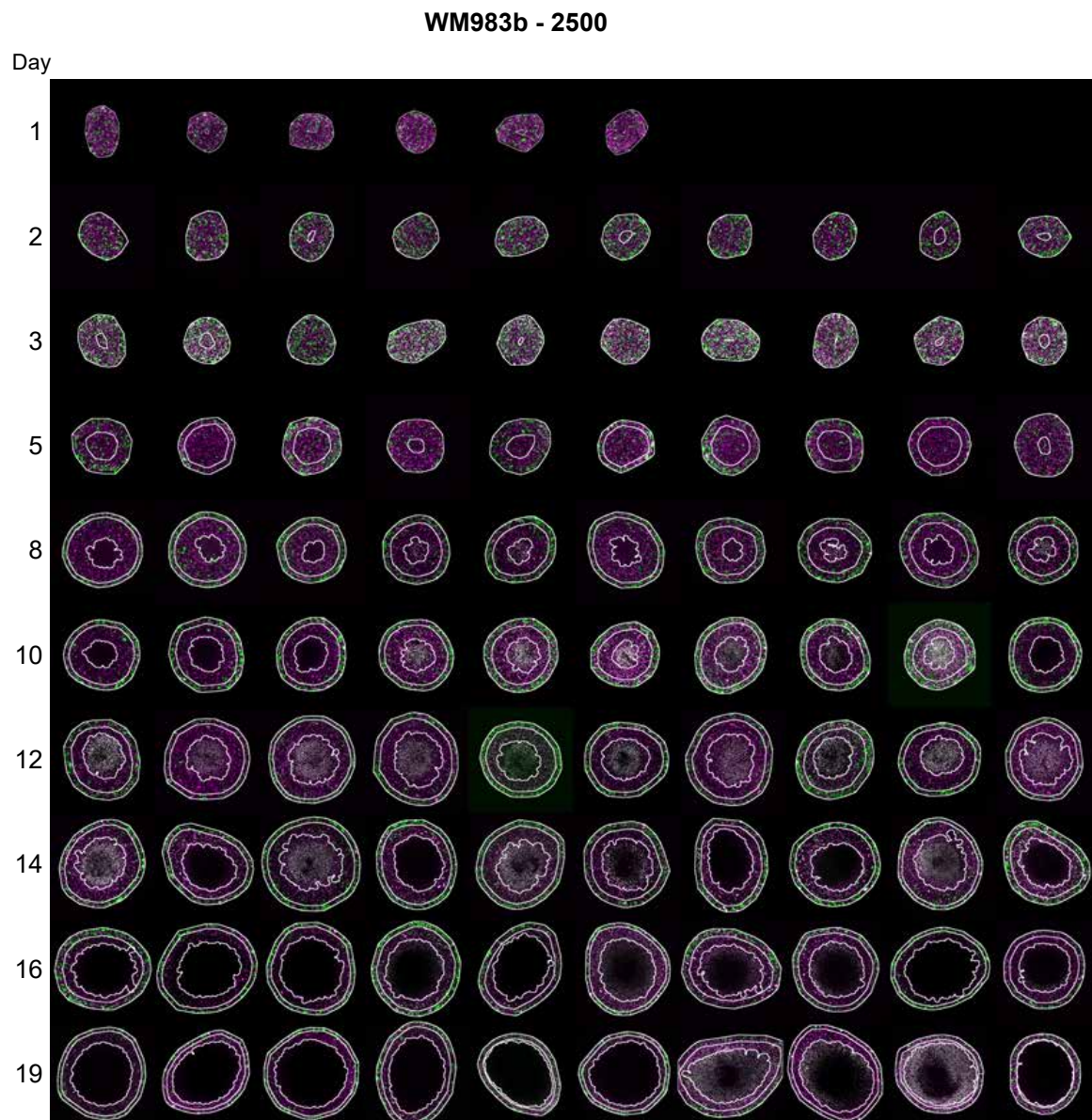


Figure S13: Experimental images of WM983b tumour spheroids formed with 2500 cells per spheroid. Each image shows a $800 \times 800 \mu\text{m}$ field of view.

WM983b - 5000

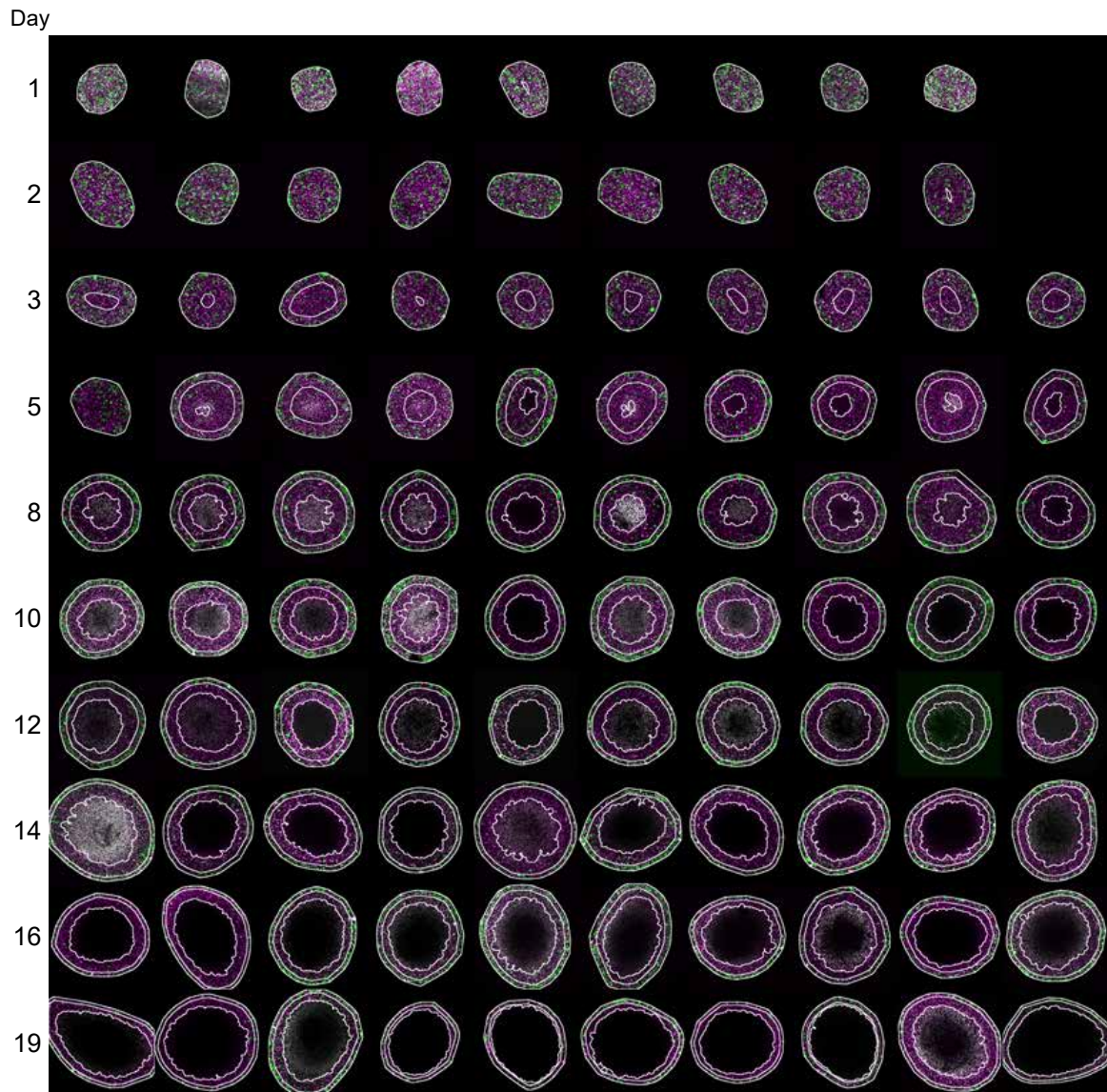


Figure S14: Experimental images of WM983b tumour spheroids formed with 5000 cells per spheroid. Each image shows a $800 \times 800 \mu\text{m}$ field of view.

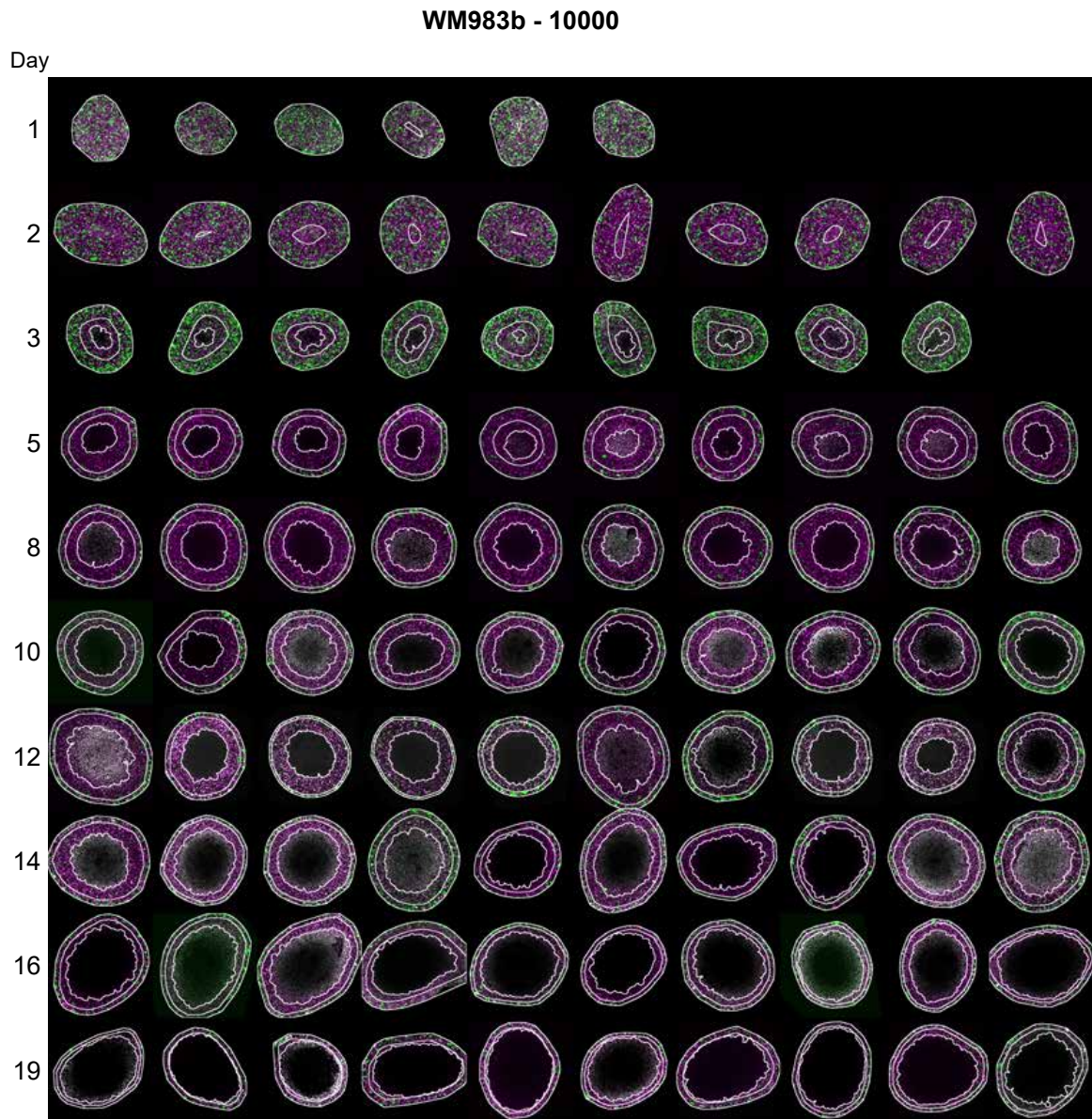


Figure S15: Experimental images of WM983b tumour spheroids formed with 10000 cells per spheroid. Each image shows a $800 \times 800 \mu\text{m}$ field of view.

C.3.3 WM164

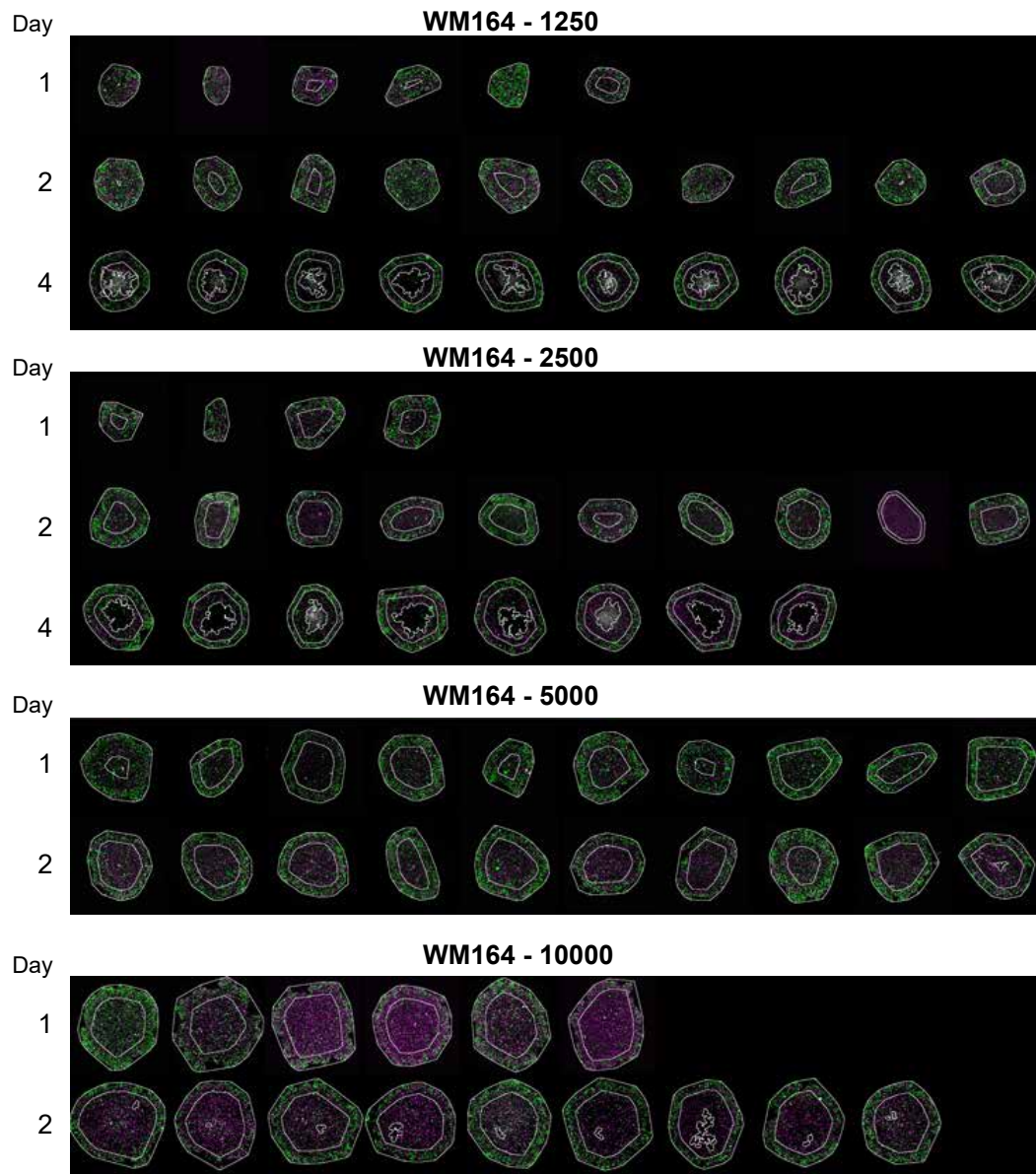


Figure S16: Experimental images of WM164 tumour spheroids formed with 1250, 2500, 5000, and 10000 cells per spheroid. Each image shows a $800 \times 800 \mu\text{m}$ field of view.

C.3.4 3D rendering

Here we present a 3D rendering of a confocal microscopy image z-stack of half of a FUCCI-melanoma WM793b spheroid 17 days after formation with 5000 cells.

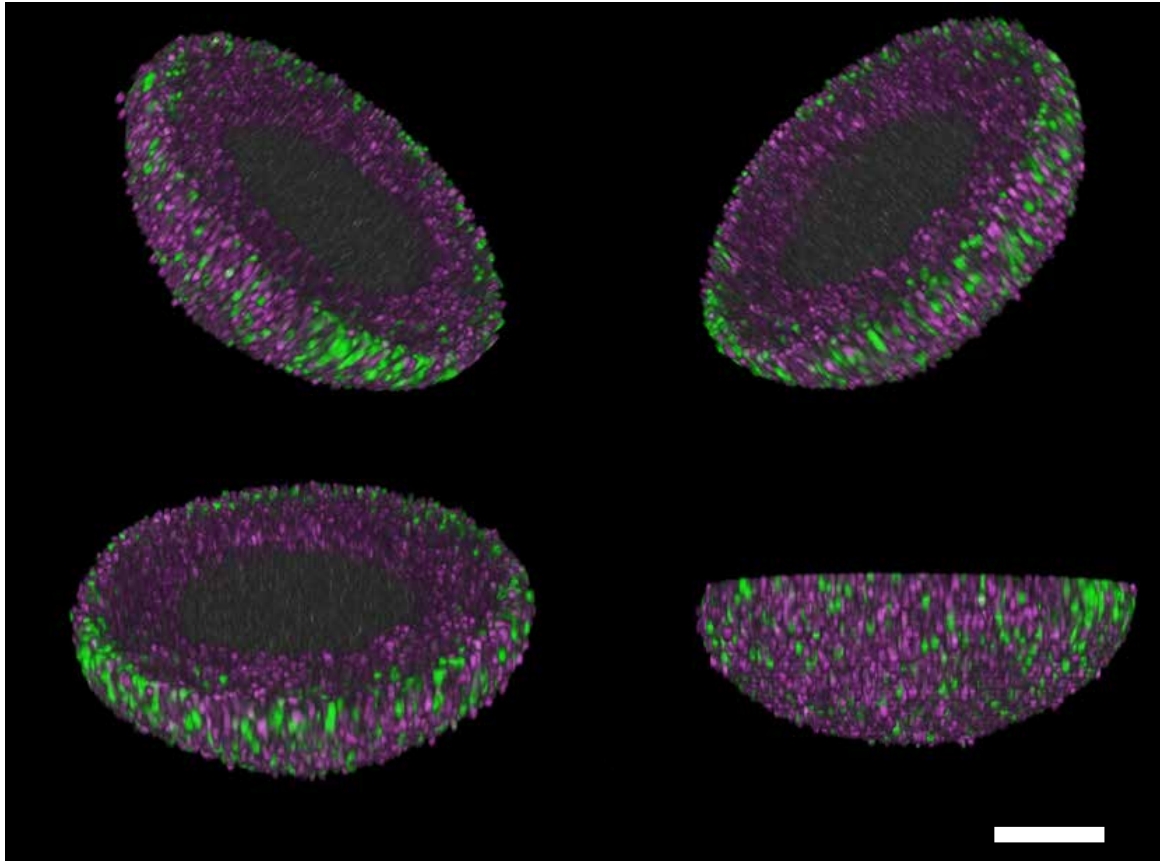


Figure S17: 3D rendering of half of a FUCCI-melanoma WM793b spheroid 17 days after formation with 5000 cells. Scale bar 200 μm .

D WM793b additional results

D.1 Results in tables

In all figures with profile likelihoods we include a red-dashed horizontal line at 0.15 indicating the 95% confidence interval threshold value [10]. Here, in Table S3 we present the corresponding MLE's and approximate 95% confidence intervals for a range of experimental designs.

Cell line	Figure	Experimental Design	Q	γ	s [day ⁻¹]	R_c [μm]	$R_o(0)$ [μm]
WM793b	2	1 Res A	0.711 (0.479, 1.000)	0.020 (0.010, 6.000)	0.141 (0.127, 1.000)	299.980 (25.000, 350.000)	183.509 (179.118, 186.825)
		1 Res B	0.675 (0.550, 1.000)	0.010 (0.010, 6.000)	0.143 (0.128, 0.324)	312.725 (85.574, 350.000)	182.940 (178.565, 186.470)
		1 Res C	0.885 (0.609, 1.000)	0.484 (0.010, 6.000)	0.134 (0.128, 0.144)	258.100 (203.186, 350.000)	183.415 (181.221, 185.260)
WM793b	3	2 Res A	1.000 (0.940, 1.000)	0.924 (0.299, 1.262)	0.126 (0.121, 0.133)	257.056 (254.484, 259.373)	184.543 (181.892, 187.082)
		3 Res A	0.770 (0.753, 0.784)	0.010 (0.010, 0.110)	0.159 (0.153, 0.166)	260.672 (257.408, 262.899)	178.733 (176.178, 181.102)
WM793b	4	3 Res A 1250 MLE	0.847 (0.824, 0.869)	0.010 (0.010, 6.000)	0.134 (0.126, 0.141)	250.352 (243.485, 256.425)	126.100 (122.459, 129.875)
		3 Res A 2500 MLE	0.829 (0.817, 0.838)	0.010 (0.010, 0.641)	0.150 (0.145, 0.157)	256.818 (253.607, 259.141)	143.797 (141.164, 146.444)
		3 Res A 5000 MLE	0.770 (0.753, 0.784)	0.010 (0.010, 0.110)	0.159 (0.153, 0.166)	260.672 (257.408, 262.899)	178.733 (176.178, 181.102)
		3 Res A 10000 MLE	0.832 (0.816, 0.846)	1.130 (0.919, 1.333)	0.149 (0.139, 0.161)	253.692 (251.158, 255.826)	223.118 (219.825, 226.245)
WM983b	S39	3 Res A 2500 MLE	0.801 (0.779, 0.822)	0.395 (0.334, 0.457)	0.319 (0.304, 0.336)	209.774 (205.679, 214.047)	128.274 (125.128, 131.309)
		3 Res A 5000 MLE	0.824 (0.815, 0.832)	0.398 (0.366, 0.445)	0.316 (0.300, 0.333)	210.220 (208.168, 212.156)	155.949 (152.684, 159.075)
		3 Res A 10000 MLE	0.841 (0.818, 0.862)	0.517 (0.475, 0.562)	0.368 (0.341, 0.398)	209.470 (205.893, 212.974)	187.514 (183.013, 191.669)
WM164	S40	3 Res A 1250 MLE	0.891 (0.856, 0.923)	0.010 (0.010, 0.408)	0.430 (0.398, 0.465)	325.842 (315.384, 335.715)	230.322 (222.762, 238.128)
		3 Res A 2500 MLE	0.813 (0.779, 0.842)	0.010 (0.010, 1.006)	0.419 (0.383, 0.487)	357.305 (351.641, 363.356)	275.862 (263.881, 285.260)
		3 Res A 5000 MLE	0.735 (0.530, 0.770)	1.365 (0.010, 6.000)	0.380 (0.298, 0.478)	434.753 (428.901, 600.000)	355.357 (339.002, 370.630)
		3 Res A 10000 MLE	0.701 (0.665, 0.736)	0.127 (0.010, 6.000)	0.287 (0.226, 0.394)	528.532 (519.431, 538.034)	471.672 (450.601, 488.117)

Table S3: Most likely estimates and approximate 95% confidence intervals for a range of experimental designs. Results shown to three decimal places.

D.2 Measurement times and experimental duration

Figure 1 shows that varying the temporal resolution in Design 1 is not sufficient to predict necrotic and inhibited radii. Here, in Figures S18 and S19, we show that varying the temporal resolution using Designs 2 and 3, respectively, gives consistent results across temporal resolutions A, B, and C.

Next we consider four additional experimental designs that use different temporal measurements

- Temporal Resolution D: the first 4 days (Day 1, 2, 3),
- Temporal Resolution E: the first 10 days (Day 1, 2, 3, 4, 5, 6, 7, 8, 9, 10),
- Temporal Resolution F: the last 10 days (Day 10, 11, 12, 13, 14, 15, 16, 17, 18, 19),
- Temporal Resolution G: the last 4 days (Day 16, 17, 18, 19),

In Figures S20 and S21, we present results for the WM793b cell line for spheroids formed with 1250 and 5000 cells, respectively. These results show that using Temporal Resolution D is not sufficient to predict late time behaviour (Figure S20e, Figure S21e) and Temporal Resolution E can also not be sufficient to predict late time behaviour (Figure S20f). Similarly, using late time experimental measurements, as in Temporal Resolutions F and G, is insufficient to determine tumour spheroid structure at early times (Figure S21g-h).

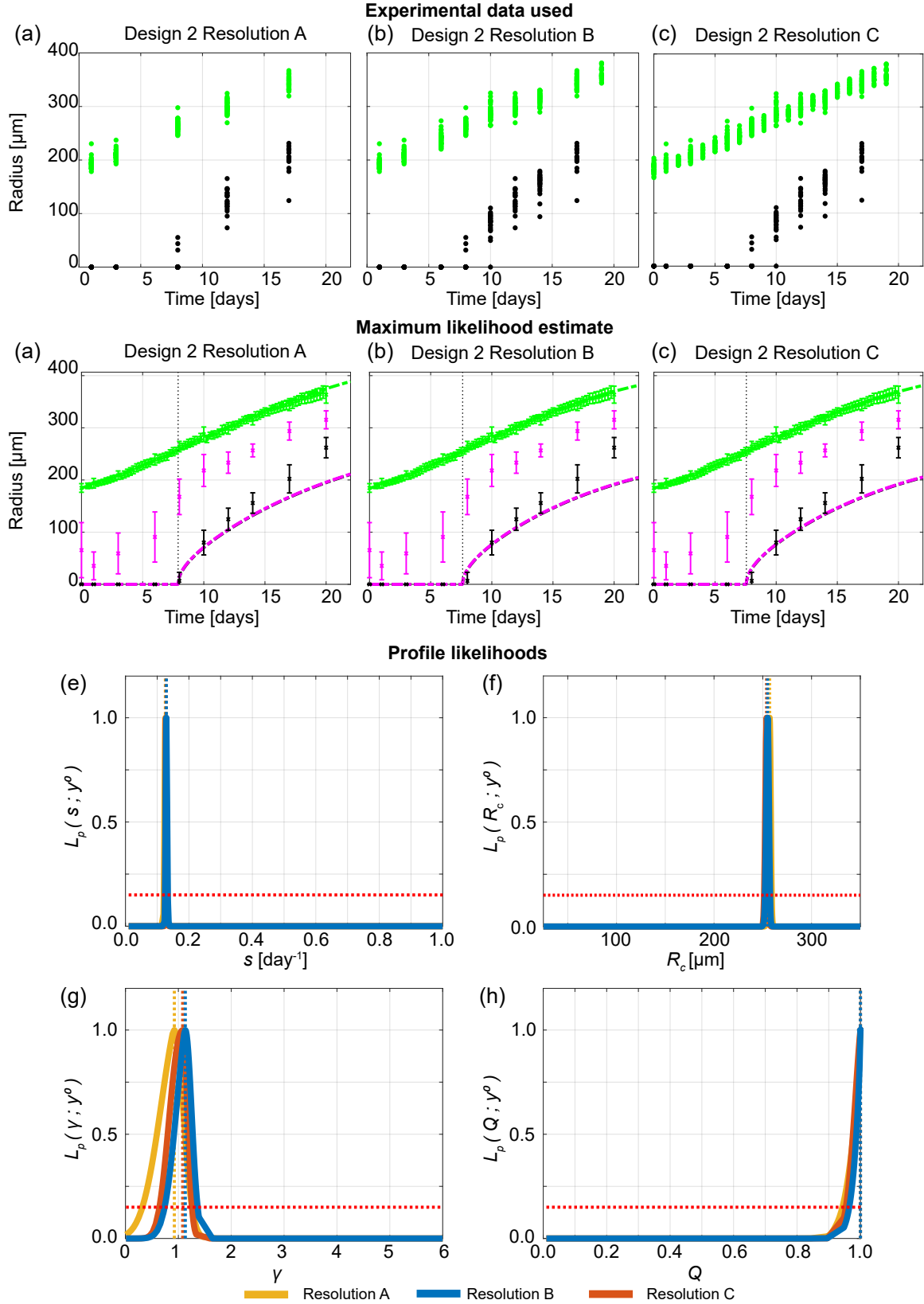


Figure S18: Increasing times when outer and necrotic radius is measured gives consistent information. (a)-(c) Experimental data used in Designs 2 with Temporal Resolutions A, B, and C. Profile likelihoods for (e) R_c , (f) s , (g) γ , (h) Q . Yellow, blue, and orange lines in (e)-(h) represent profile likelihoods from Design 2 with Temporal Resolutions A, B, and C, respectively. (i)-(k) Comparison of Greenspan model simulated with maximum likelihood estimate compared to full experimental data set for Design 2 with Temporal Resolutions A, B, and C, where error bars show standard deviation.

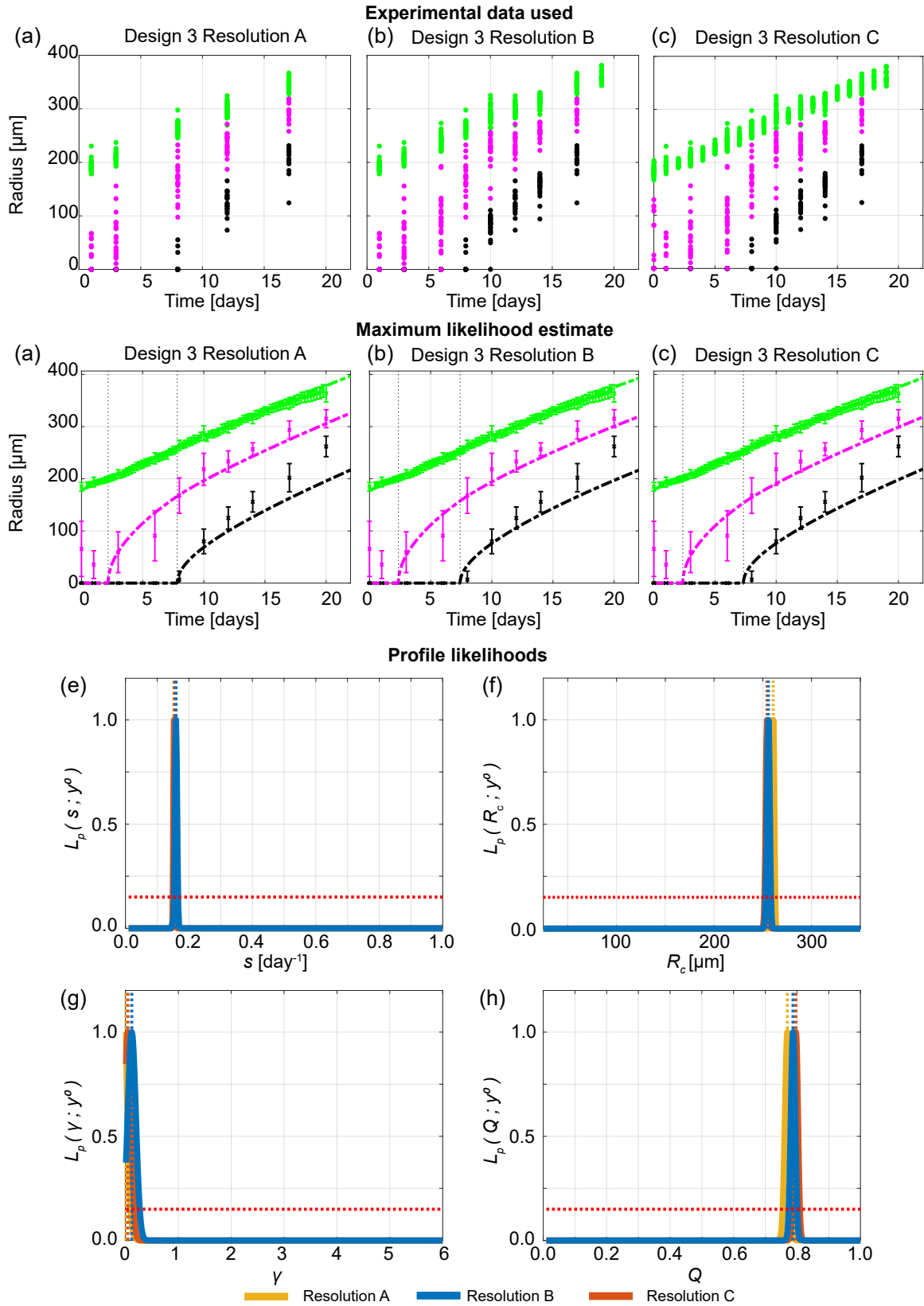


Figure S19: Increasing times when outer, necrotic and inhibited radius and necrotic is measured gives consistent information. (a)-(c) Experimental data used in Designs 3 with Temporal Resolutions A, B, and C. Profile likelihoods for (e) R_c , (f) s , (g) γ , (h) Q . Yellow, blue, and orange lines in (e)-(h) represent profile likelihoods from Design 3 with Temporal Resolutions A, B, and C, respectively. (i)-(k) Comparison of Greenspan model simulated with maximum likelihood estimate compared to full experimental data set for Design 3 with Temporal Resolutions A, B, and C, where error bars show standard deviation.

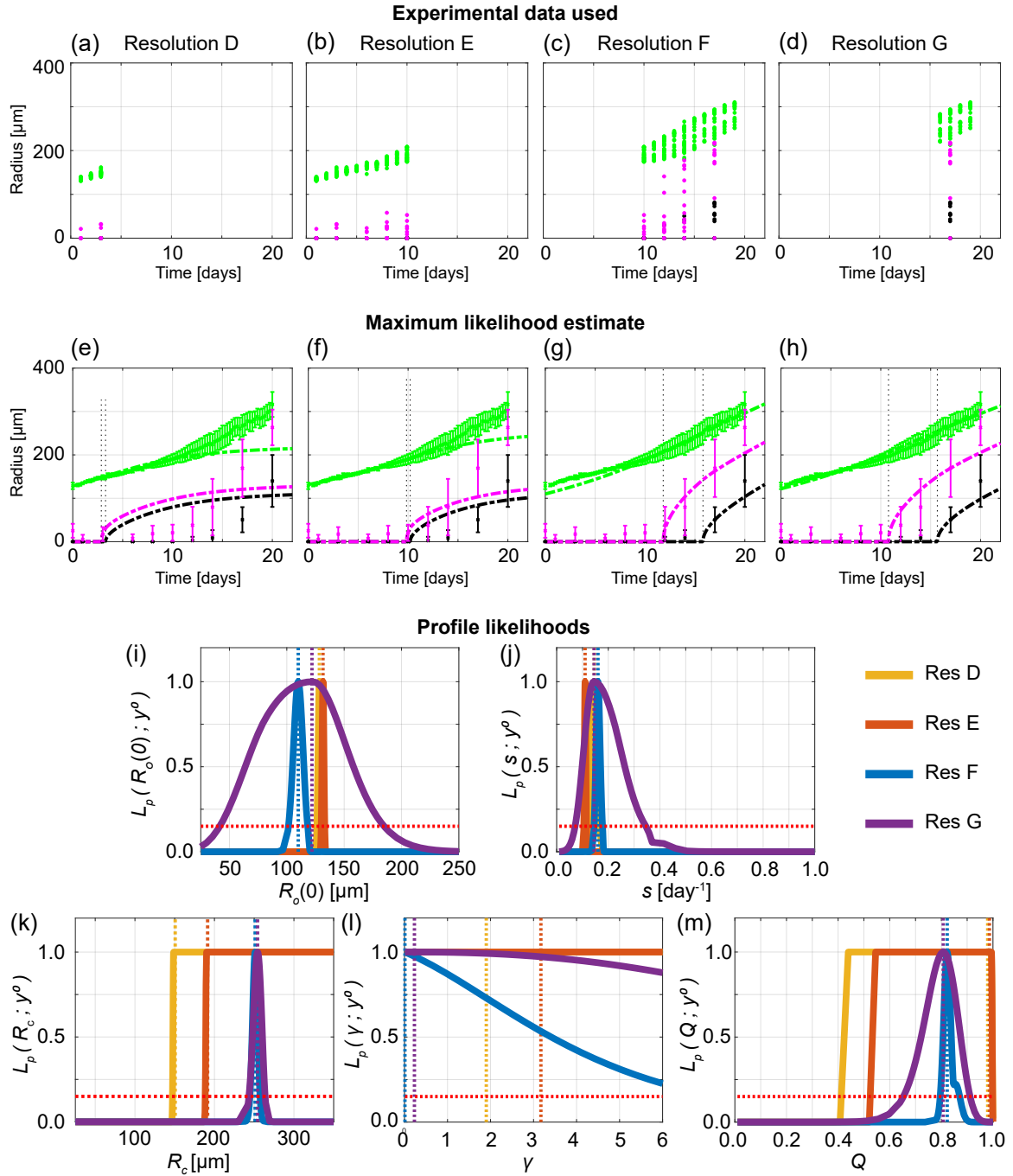


Figure S20: Design 3 with temporal Resolutions D, E, F, and G for WM793b tumour spheroids formed with 1250 cells per spheroid. (a)-(d) Experimental data used in Designs 3 Temporal Resolutions D, E, F, and G. (e)-(h) Comparison of Greenspan model simulated with maximum likelihood estimate compared to full experimental data set for Designs 3 Temporal Resolutions D, E, F, and G, where error bars show standard deviation. Profile likelihoods for (i) $R_o(0)$, (j) s , (k) R_c , (l) γ , (m) Q . Yellow, orange, blue, and purple lines in (e)-(h) represent profile likelihoods from Designs 3 Temporal Resolutions D, E, F, and G, respectively.

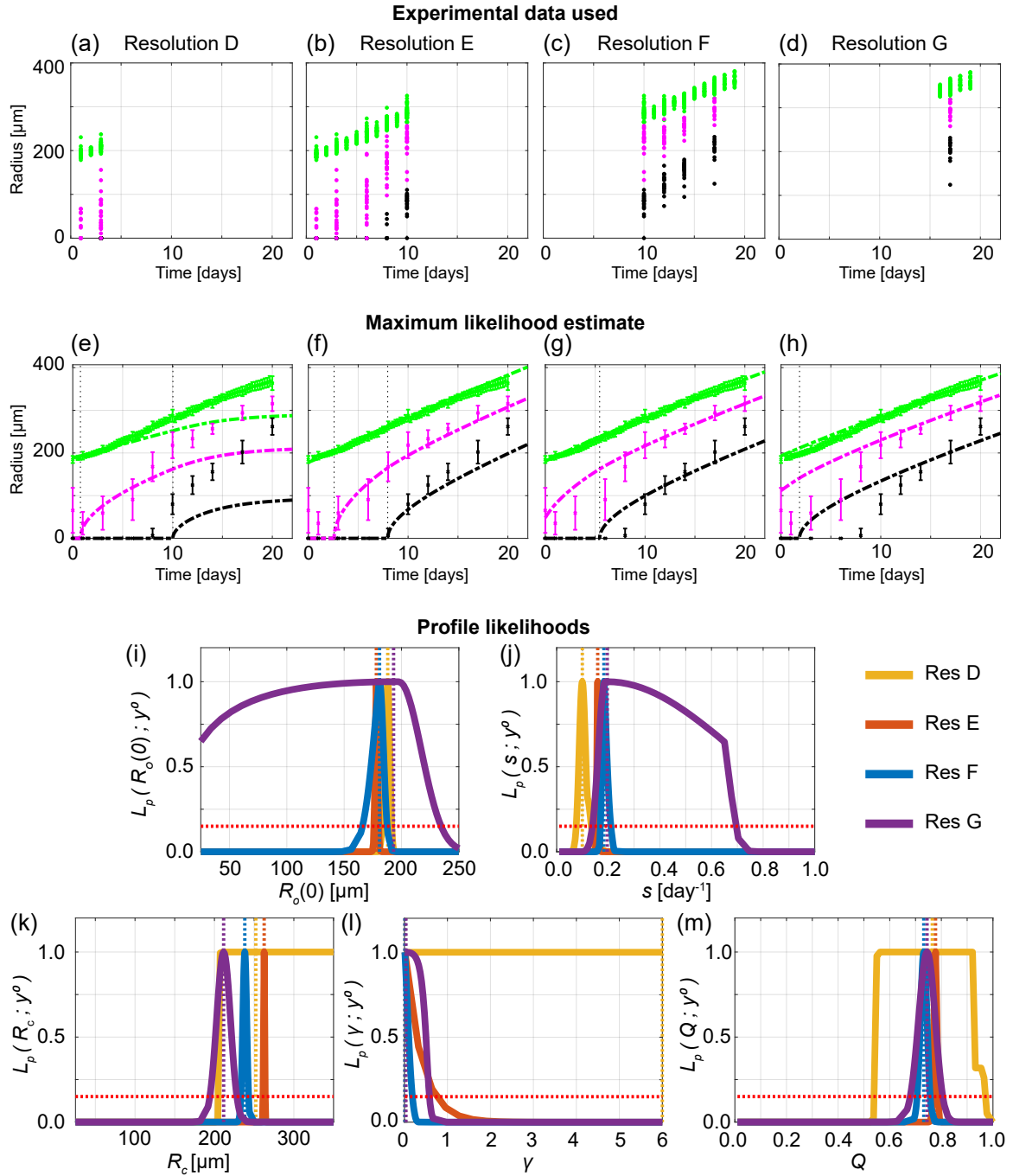


Figure S21: Design 3 with temporal Resolutions D, E, F, and G for WM793b tumour spheroids formed with 5000 cells per spheroid. (a)-(d) Experimental data used in Designs 3 Temporal Resolutions D, E, F, and G. (e)-(h) Comparison of Greenspan model simulated with maximum likelihood estimate compared to full experimental data set for Designs 3 Temporal Resolutions D, E, F, and G, where error bars show standard deviation. Profile likelihoods for (i) $R_o(0)$, (j) s , (k) R_c , (l) γ , (m) Q . Yellow, orange, blue, and purple lines in (e)-(h) represent profile likelihoods from Designs 3 Temporal Resolutions D, E, F, and G, respectively.

D.3 Profile likelihoods for $R_o(0)$

To perform statistical identifiability analysis we treat the initial outer radius, $R_o(0)$, as a parameter. Here, in Figure S22 we show that profile likelihoods for $R_o(0)$ are consistent across temporal resolutions and experimental designs.

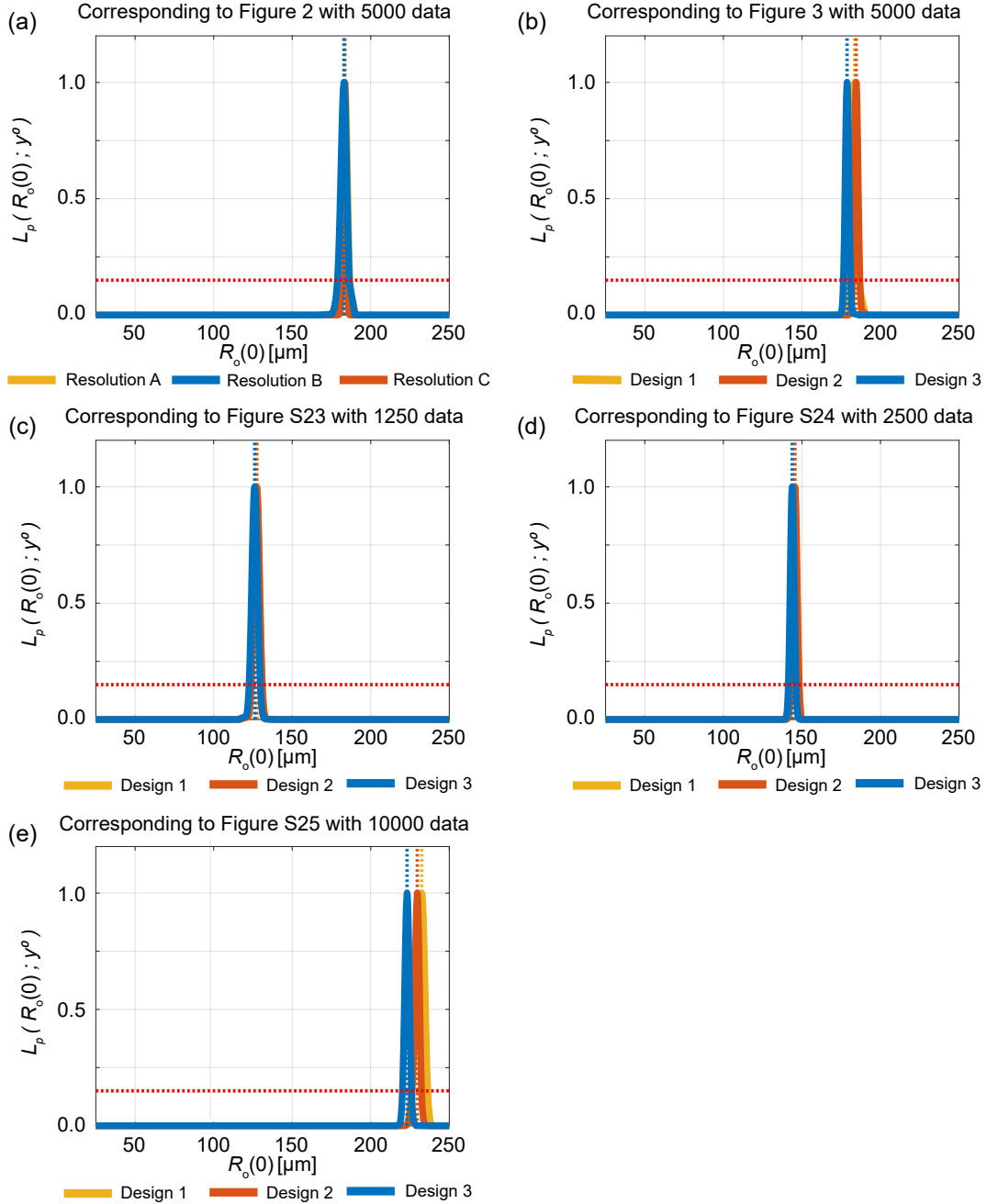


Figure S22: Profile likelihoods for $R_o(0)$

D.4 Outer radius measurements are not sufficient to predict inhibited and necrotic radii

In Figure 2 we compare Design 1 with Temporal Resolutions A, B, and C for the WM793b cell line formed with 5000 cells. Here, in Figures S23, S24, and S25, we compare Designs 1 with Temporal Resolutions A, B, and C for the WM793b spheroids formed with 1250, 2500, and 10000 cells, respectively. These results show that Design 1 is not a reliable design and that outer radius measurements are not sufficient to predict inhibited and necrotic radii.

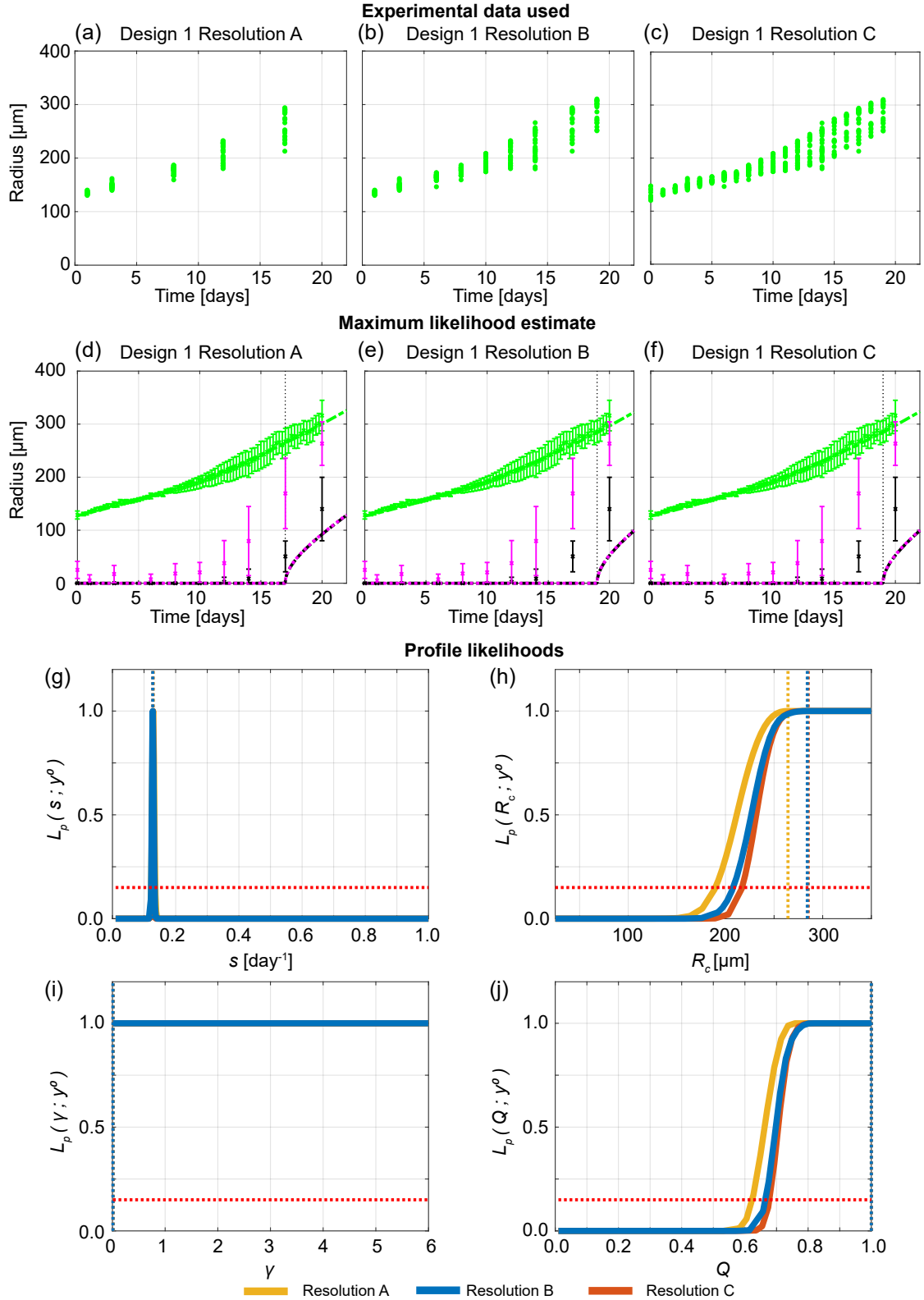


Figure S23: Increasing the temporal resolution when the outer radius is measured does not provide accurate information on internal structure. (a)-(c) Experimental data used in Design 1 with temporal resolutions A, B, and C. (d)-(f) Comparison of Greenspan model simulated with maximum likelihood estimate compared to full experimental data set, where error bars show standard deviation. Profile likelihoods for (g) s , (h) R_c , (i) γ , (j) Q . Yellow, blue, orange lines in (g)-(j) represent profile likelihoods from Design 1 with temporal resolutions A, B, and C, respectively, and the red-dashed line shows the approximate 95% confidence interval threshold. Results shown for WM793b spheroids formed with 1250 cells per spheroid.

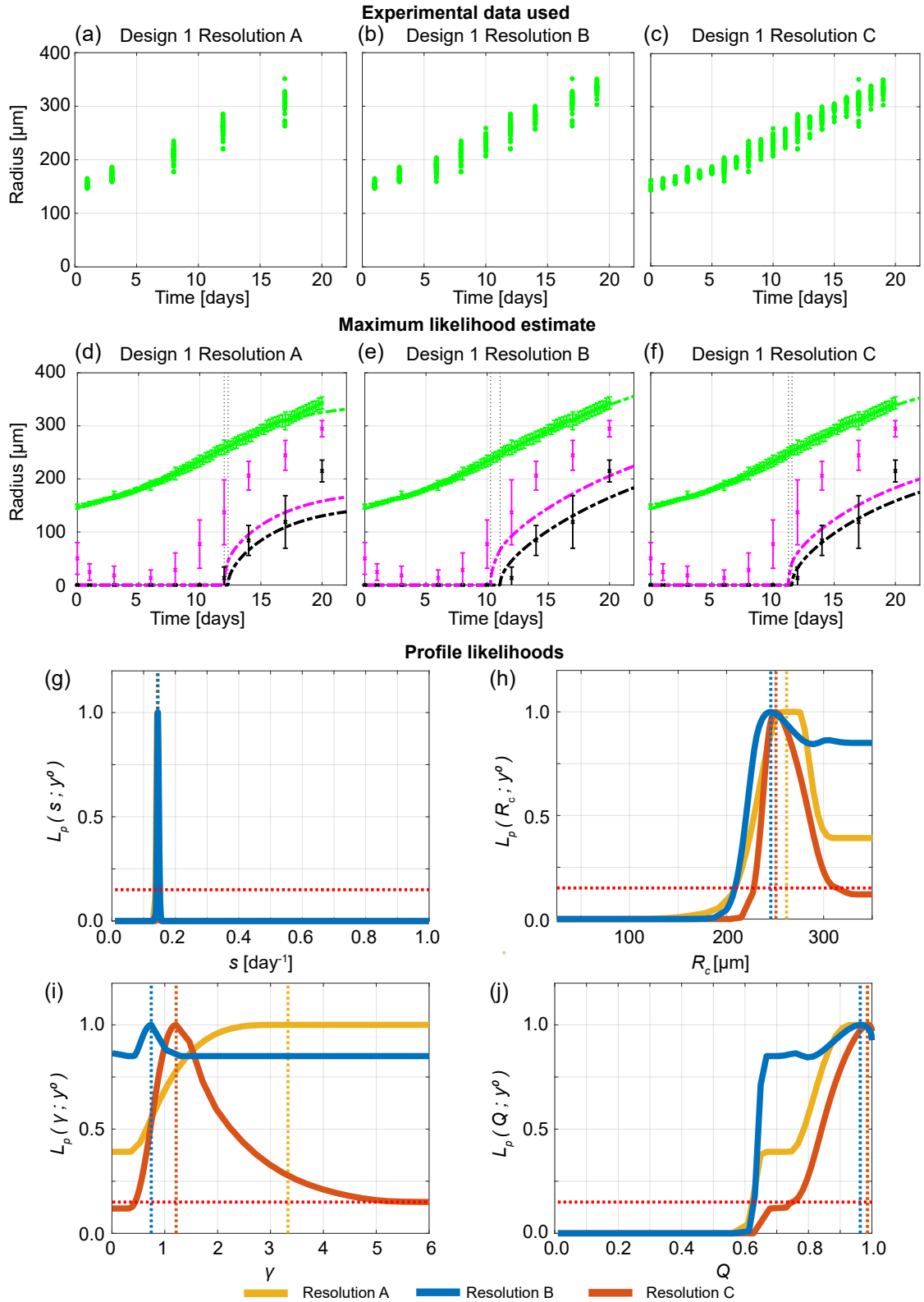


Figure S24: Increasing the temporal resolution when the outer radius is measured does not provide accurate information on internal structure. (a)-(c) Experimental data used in Design 1 with temporal resolutions A, B, and C. (d)-(f) Comparison of Greenspan model simulated with maximum likelihood estimate compared to full experimental data set, where error bars show standard deviation. Profile likelihoods for (g) s , (h) R_c , (i) γ , (j) Q . Yellow, blue, orange lines in (g)-(j) represent profile likelihoods from Design 1 with temporal resolutions A, B, and C, respectively, and the red-dashed line shows the approximate 95% confidence interval threshold. Results shown for WM793b spheroids formed with 2500 cells per spheroid.

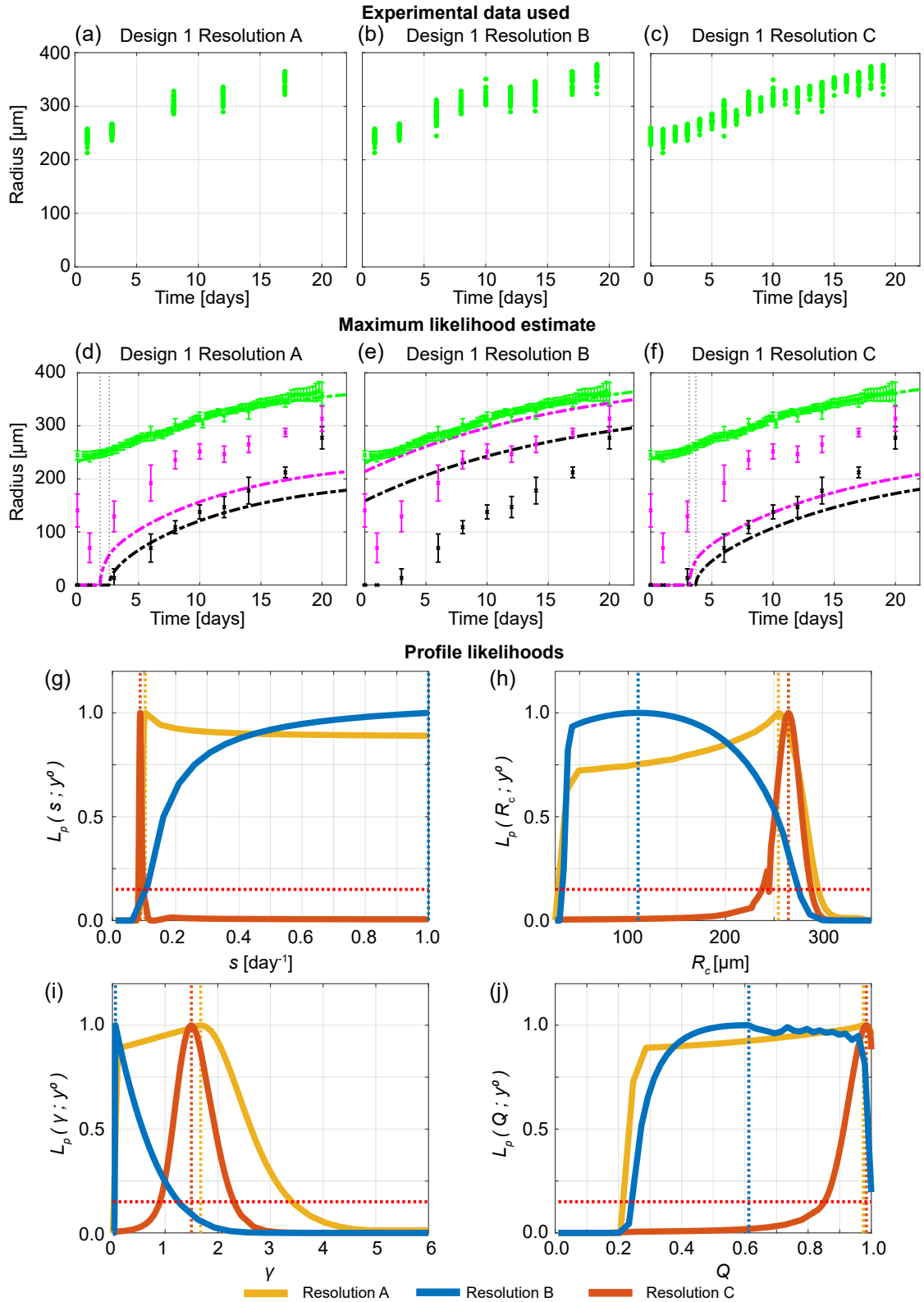


Figure S25: Increasing the temporal resolution when the outer radius is measured does not provide accurate information on internal structure. (a)-(c) Experimental data used in Design 1 with temporal resolutions A, B, and C. (d)-(f) Comparison of Greenspan model simulated with maximum likelihood estimate compared to full experimental data set, where error bars show standard deviation. Profile likelihoods for (g) s , (h) R_c , (i) γ , (j) Q . Yellow, blue, orange lines in (g)-(j) represent profile likelihoods from Design 1 with temporal resolutions A, B, and C, respectively, and the red-dashed line shows the approximate 95% confidence interval threshold. Results shown for WM793b spheroids formed with 10000 cells per spheroid.

D.5 Cell cycle data are informative

In Figure 3 we compare Designs 1, 2, and 3 for the WM793b cell line formed with 5000 cells. Here, in Figures S26, S27, and S28, we compare Designs 1, 2, and 3 for the WM793b spheroids formed with 1250, 2500, and 10000 cells, respectively. These results also show that Design 3 provides most insight.

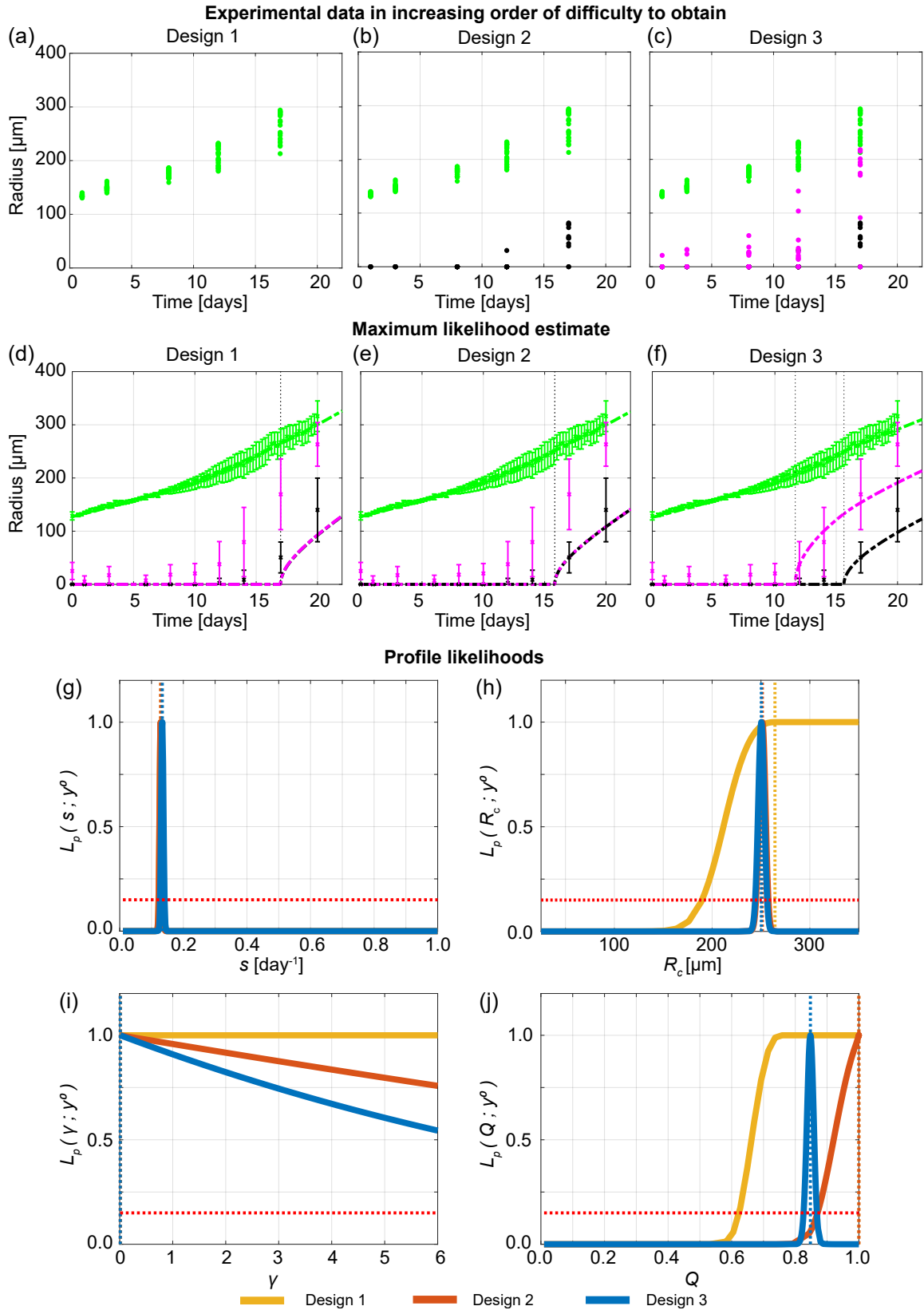


Figure S26: Measuring the necrotic and inhibited radius provides valuable information. (a)-(b) Experimental data used in Designs 2 and 3. (c)-(d) Comparison of Greenspan model simulated with maximum likelihood estimate compared to full experimental data set for Designs 2 and 3, where error bars show standard deviation. Profile likelihoods for (e) s , (f) R_c , (g) γ , (h) Q . Yellow, orange, blue lines in (e)-(h) represent profile likelihoods from Designs 1, 2, and 3, respectively, and the red-dashed line shows the approximate 95% confidence interval threshold. Results shown for WM793b spheroids formed with 1250 cells per spheroid.

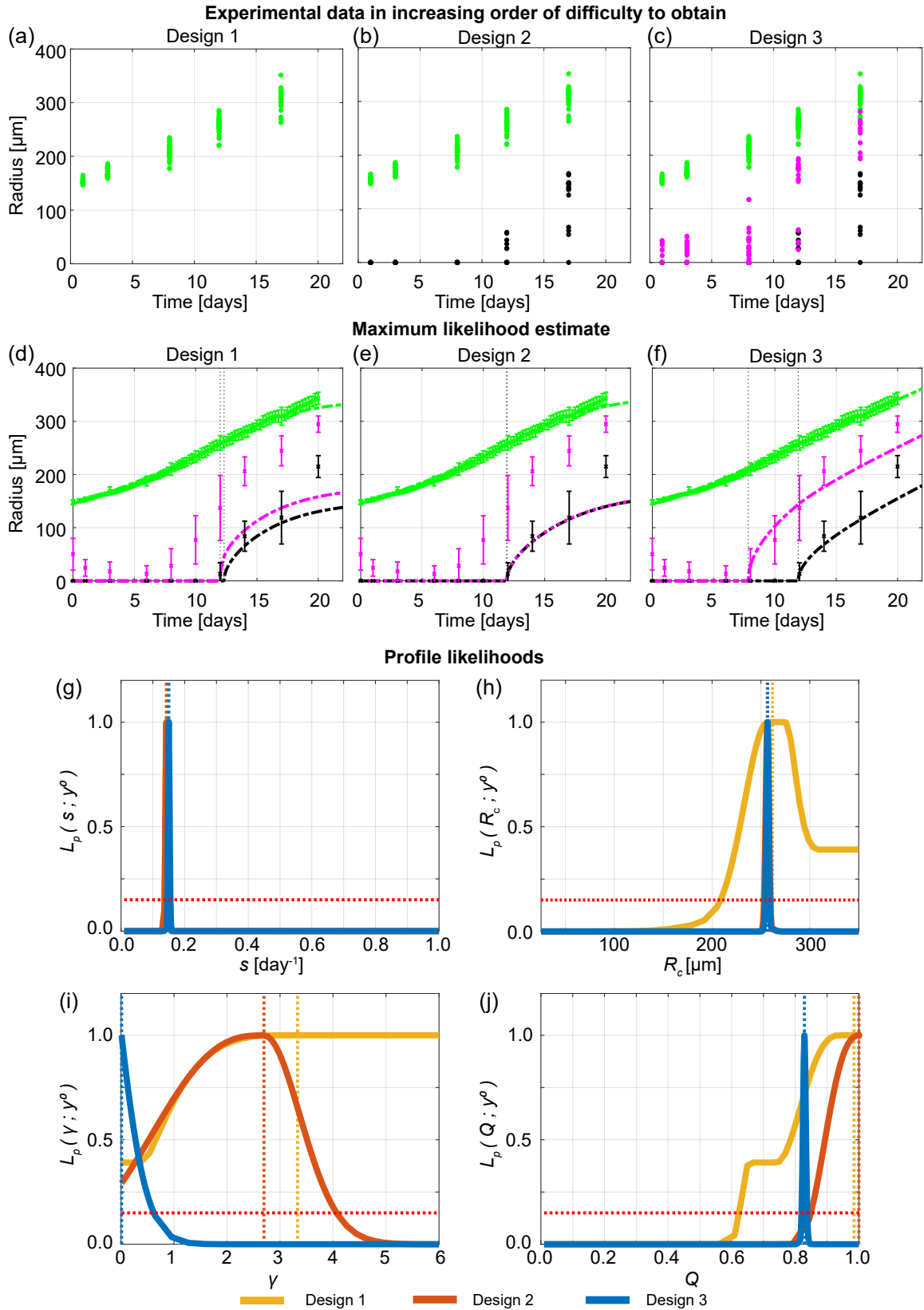


Figure S27: Measuring the necrotic and inhibited radius provides valuable information. (a)-(b) Experimental data used in Designs 2 and 3. (c)-(d) Comparison of Greenspan model simulated with maximum likelihood estimate compared to full experimental data set for Designs 2 and 3, where error bars show standard deviation. Profile likelihoods for (e) s , (f) R_c , (g) γ , (h) Q . Yellow, orange, blue lines in (e)-(h) represent profile likelihoods from Designs 1, 2, and 3, respectively, and the red-dashed line shows the approximate 95% confidence interval threshold. Results shown for WM793b spheroids formed with 2500 cells per spheroid.

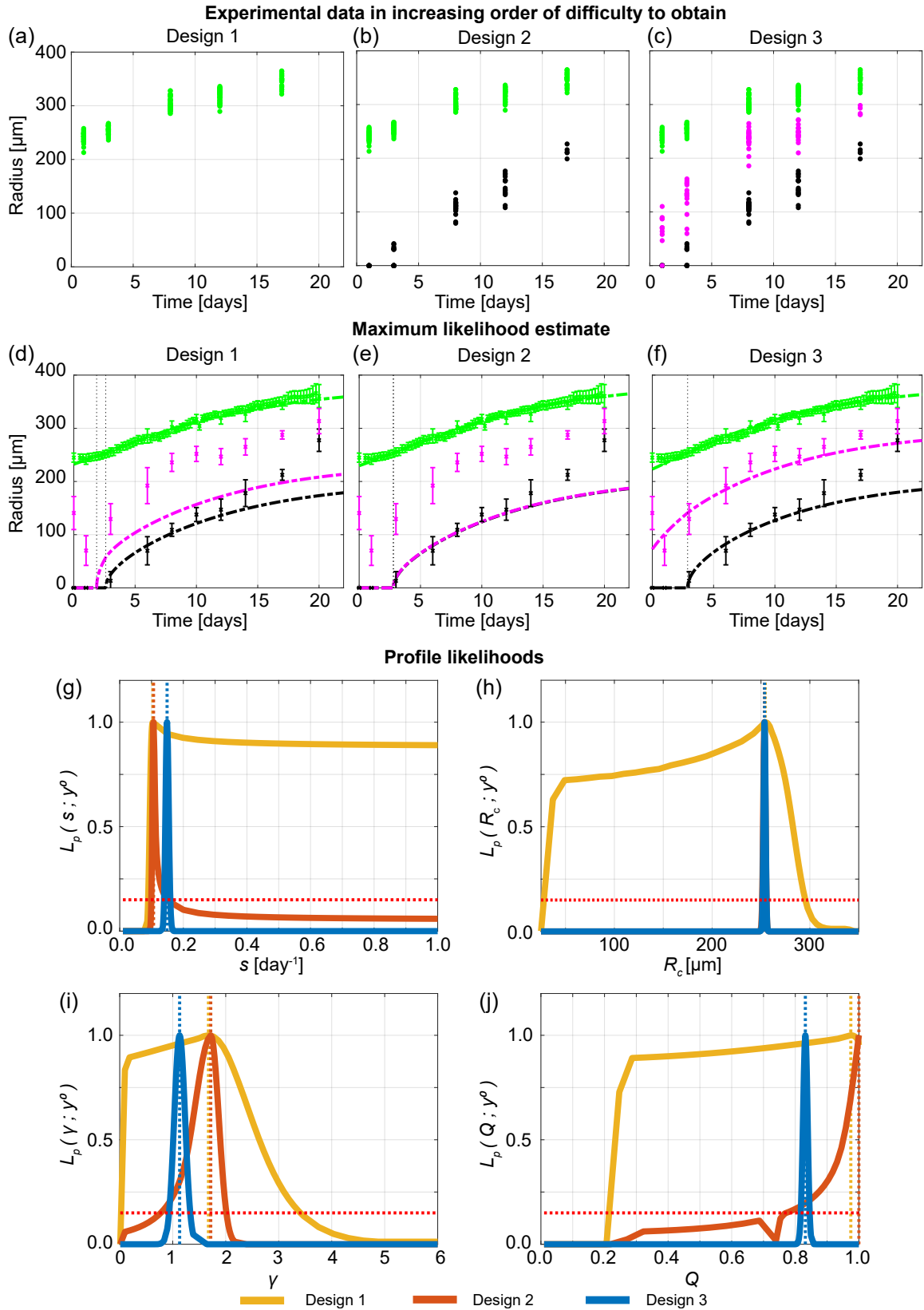


Figure S28: Measuring the necrotic and inhibited radius provides valuable information. (a)-(b) Experimental data used in Designs 2 and 3. (c)-(d) Comparison of Greenspan model simulated with maximum likelihood estimate compared to full experimental data set for Designs 2 and 3, where error bars show standard deviation. Profile likelihoods for (e) s , (f) R_c , (g) γ , (h) Q . Yellow, orange, blue lines in (e)-(h) represent profile likelihoods from Designs 1, 2, and 3, respectively, and the red-dashed line shows the approximate 95% confidence interval threshold. Results shown for WM793b spheroids formed with 10000 cells per spheroid.

E Synthetic data: WM793b

To confirm that profile likelihood analysis works as expected, we generate synthetic data from Greenspan’s model using known parameters. We then explore when these known parameters are recovered using the varying experimental designs considered in the main manuscript: Design 1 with varying temporal resolutions (Supplementary Material E.1); comparing Design 1, Design 2 and Design 3 (Supplementary Material E.2), and exploring the role of initial spheroid size and also here experimental duration (Supplementary Material E.3). Since Greenspan’s model may be misspecified, and may not capture all of the biological details of tumour spheroid growth, the fact that these results for synthetic data are consistent with those from experimental data enhances our confidence that key biological features are captured in Greenspan’s model. Furthermore, when generating synthetic data there is additional flexibility so we also explore what may happen if we were to spend significantly more time collecting measurements (Supplementary Material E.4).

To generate synthetic data, we use the MLE from Design 3 Resolution C applied to experimental data obtained from WM793b spheroids each formed with 5000 cells: $(R_c, s, \gamma, Q, R_o(0)) = (254.366, 0.1532, 0.045, 0.797, 179.550)$. First, we simulate Greenspan’s deterministic mathematical model with these known parameters. Next, to obtain one noisy synthetic outer radius measurement we record the outer radius from Greenspan’s model generated from the known parameters at one time point. Next, we sample a normal distribution with zero mean and variance given by experimentally obtained outer radius pooled sample variance $s_o^2 = 9.35$. We add this sampled noise to the recorded outer radius measurement. We repeat this process to obtain additional outer radius measurements. Similarly, we repeat this process to obtain necrotic and inhibited radius measurements, using experimentally obtained pooled sample variances $s_n^2 = 15.89$, and $s_i^2 = 33.12$, respectively. We generate 10 measurements, or 48 when exploring the role of additional measurements in supplementary material E.4, of the outer radius, inhibited radius and necrotic radius every half day from day 0 to day 20.

E.1 Outer radius measurements are not sufficient to predict inhibited and necrotic radii

Similarly to Figure 2, we observe in Figure S29 that outer radius measurements are not sufficient to predict inhibited and necrotic radii. Simulating Greenspan’s model with the MLE from Design 1 Time Resolution A (Figure S29d) and with Design 1 Time Resolution B (Figure S29e) shows the time evolution of the outer radius is captured but the time evolution of the inhibited and necrotic region are not. However, simulating Greenspan’s model with the MLE from Design 1 Time Resolution C (Figure S29f) appears to capture the time evolution of the outer, inhibited, and necrotic radii. However, inspecting the profile likelihoods in Figures S29g-j shows that while the known parameters are captured but the profiles are wide suggesting that parameters are non-identifiable. This means that many values parameters give a similar match to the outer radius experimental data and these parameters do not necessarily agree with the inhibited and necrotic radii measurements.

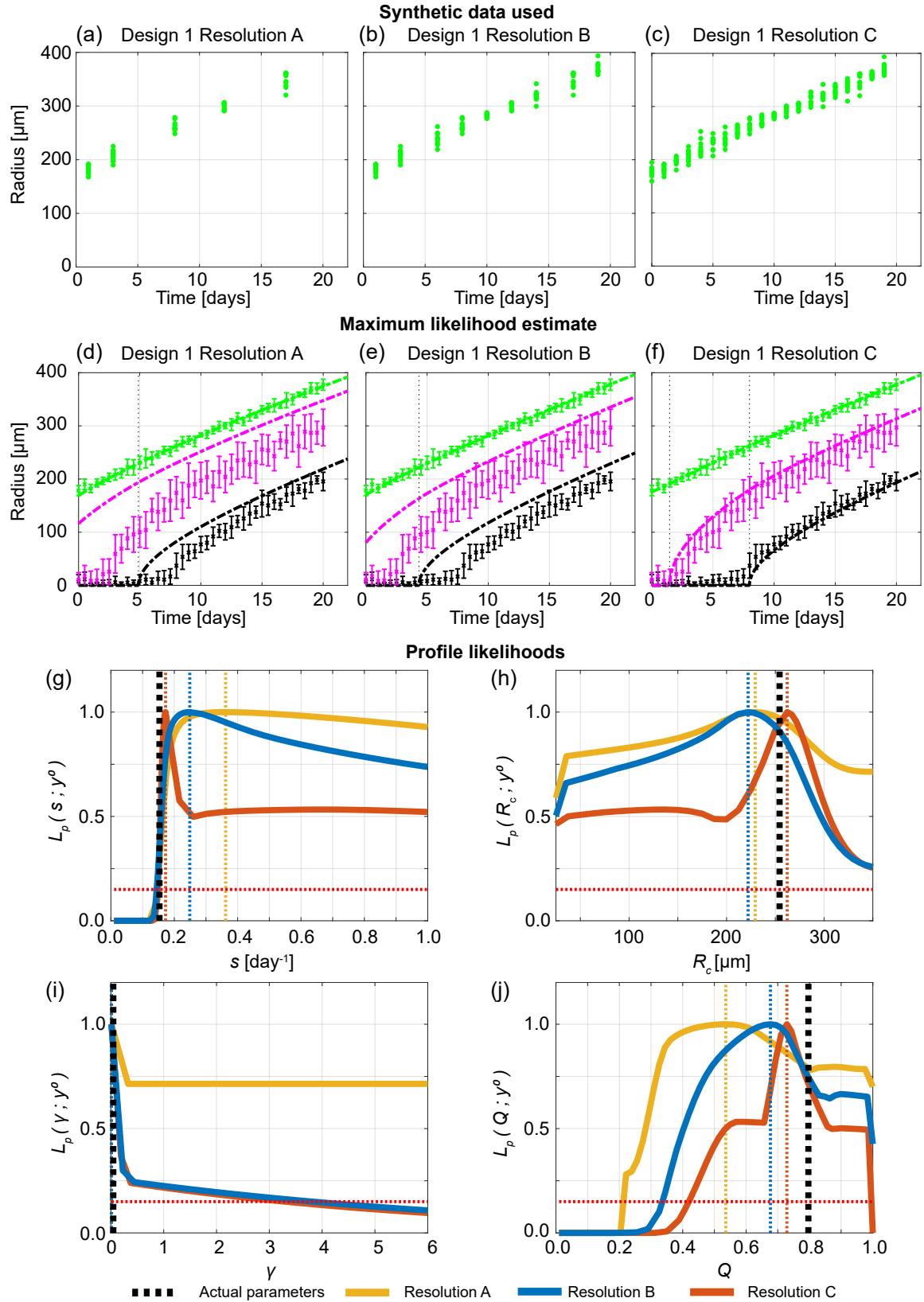


Figure S29: Synthetic data shows that outer radius measurements are not sufficient to predict inhibited and necrotic radii. (a)-(c) Synthetic data used in Designs 1 with Temporal Resolutions A, B, and C. (d)-(f) Comparison of Greenspan model simulated with maximum likelihood estimate compared to full synthetic data set. Profile likelihoods for (g) s , (h) R_c , (i) γ , (j) Q . Yellow, blue, and orange lines in (g)-(j) represent profile likelihoods from Design 1 with Temporal Resolutions A, B, and C, respectively. Black dashed lines in (g)-(j) show known parameters used to generate the synthetic data.

E.2 Cell cycle data are informative

Similarly to Figure 3, Design 3 provides most insight and best captures the known parameter values used to generate the synthetic data (Figure S30).

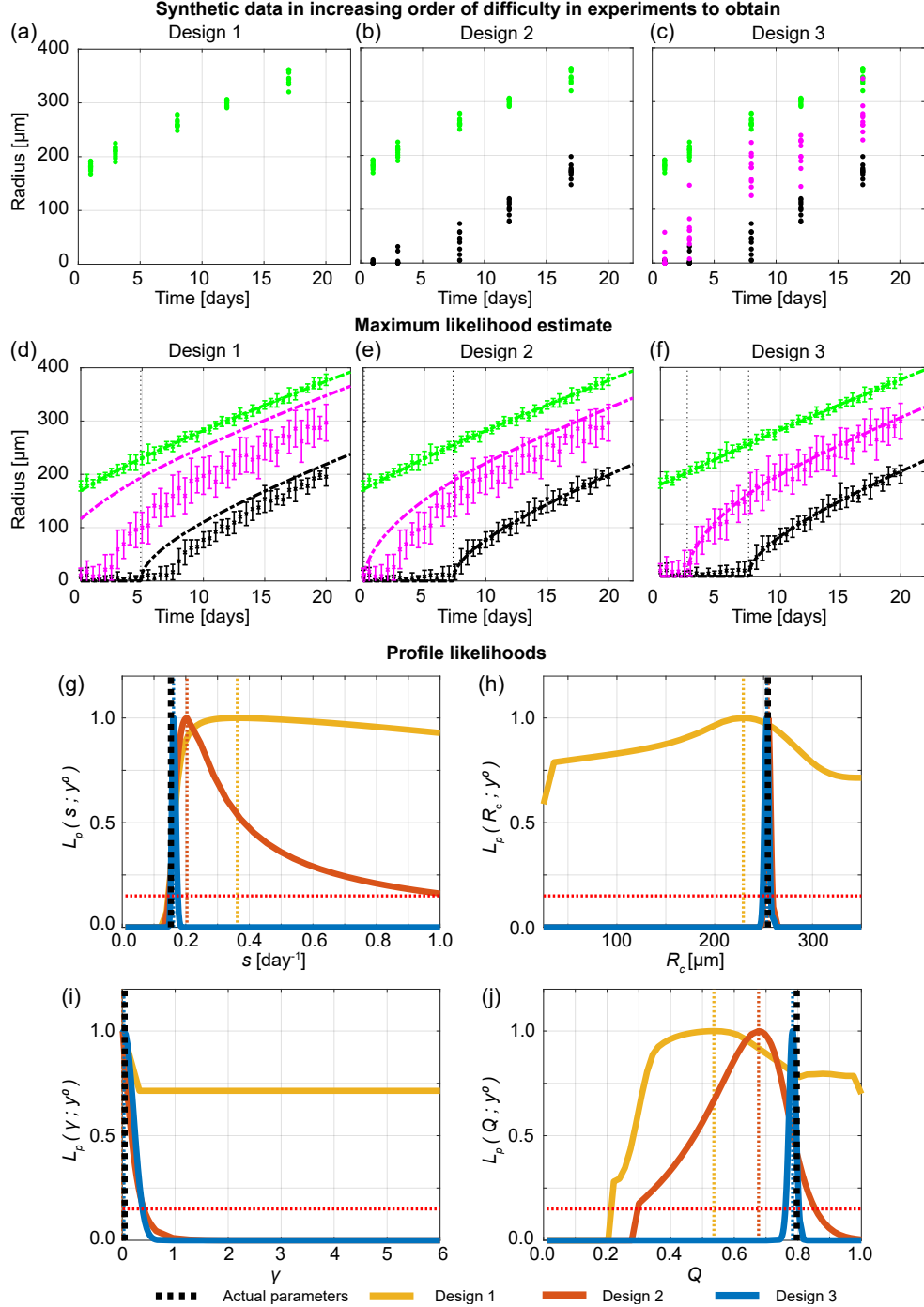


Figure S30: Synthetic data shows that measuring the necrotic and inhibited radius provides valuable information. (a)-(b) Synthetic data used in Designs 2 and 3. (c)-(d) Comparison of Greenspan model simulated with maximum likelihood estimate compared to full synthetic data set for Designs 2 and 3. Profile likelihoods for (e) s , (f) R_c , (g) γ , (h) Q . Yellow, orange, blue lines in (e)-(h) represent profile likelihoods from Designs 1 low temporal resolution, 2, and 3, respectively. Black dashed lines in (e)-(h) show known parameters used to generate the synthetic data.

E.3 Role of initial spheroid size and experiment duration

In Greenspan's model a change in the initial radius, $R_o(0)$, corresponds to a shift in time (Figure S31a). We now consider the role of initial spheroid size and experiment duration. As before, we use the MLE from spheroids formed with 5000 cells per spheroid to generate synthetic data. To generate synthetic data for spheroids formed with 1250, 2500, and 10000 cells per spheroid we use the MLE obtained from spheroids formed with 5000 cells per spheroid and only update $R_o(0)$. To update $R_o(0)$ we use the MLE from Design 3 applied to experimental data obtained from WM793b spheroids formed with 1250, 2500, and 10000 cells per spheroid, respectively.

We assume that each experiment is performed to Day 6 after formation, and use Design 3 with 10 measurements obtained on Day 1, 2, 3, 4, 5, and 6 (Figure S31b-e). Note that during this experimental duration only spheroids formed with 10000 cells per spheroid form a necrotic core with the known parameters, while only spheroids formed with 5000 and 10000 cells per spheroid form an inhibited region with the known parameters. Therefore, we expect that most insight will be gained from the experiment formed with spheroids formed with 10000 cells per spheroid.

Simulating Greenspan's model with the MLE obtained from each of those data sets (dashed lines in Figures S31f-i) we observe good agreement to the first six days of synthetic data for each initial spheroid size. However, simulating Greenspan's model with the MLE obtained from each of those data sets (dashed lines in Figures S31f-i) and comparing to Greenspan's model simulated over 20 days with the known parameters used to generate the synthetic data (solid lines in Figures S31f-i) this is not the case. We only observe excellent agreement for the experiment with spheroids formed with 10000 cells, since this experiment has measurements in phase (iii). Profile likelihoods for the parameters also show that only the experiment performed with spheroids formed with 10000 cells accurately captures the known parameters (Figure S31j-n).

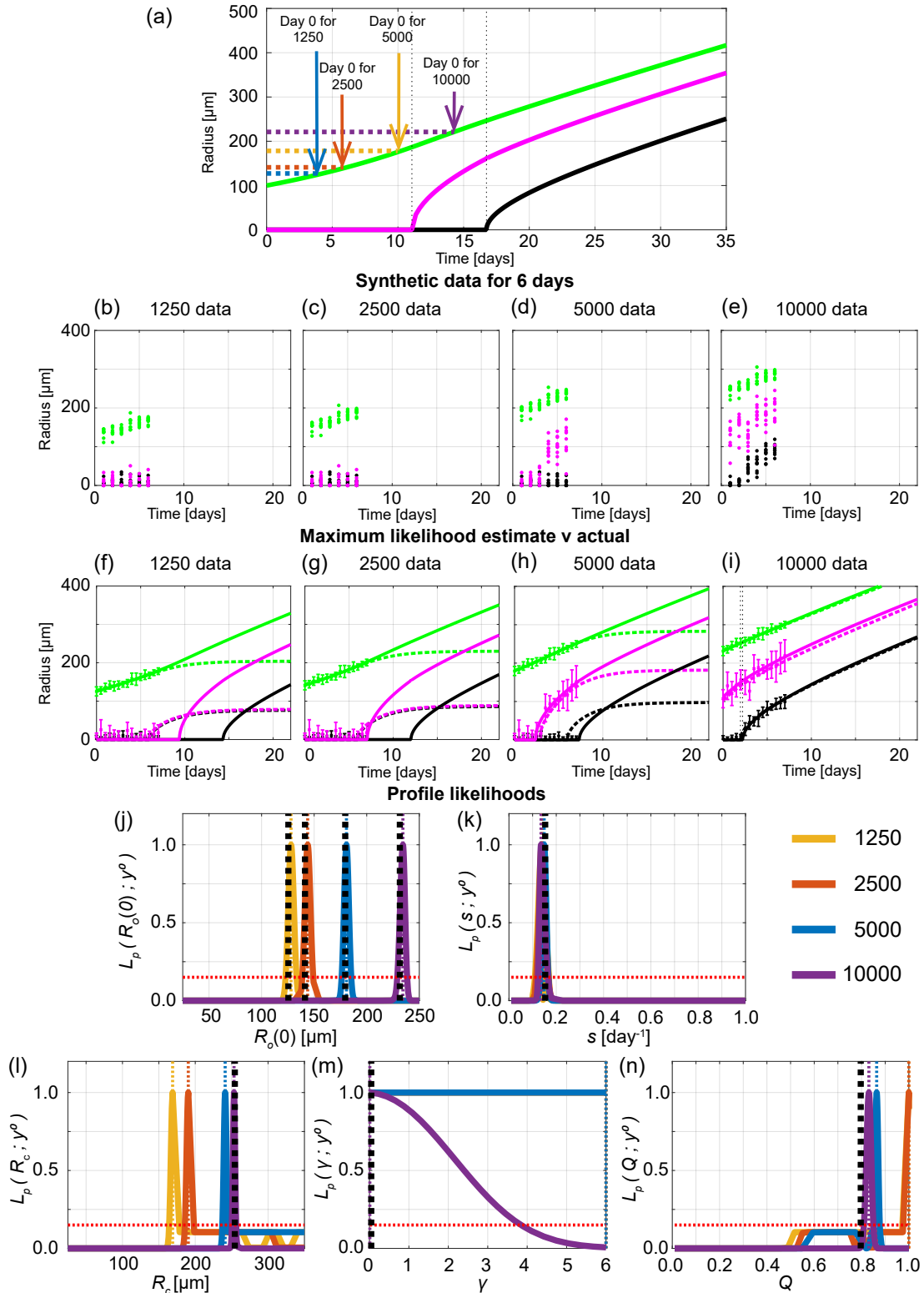


Figure S31: Synthetic data exploring role of initial spheroid size and experimental duration. (a) In Greenspan's model a change in $R_o(0)$ corresponds to a shift in time. (b)-(d) Synthetic generated for the first six days after formation for spheroids formed with (b) 1250, (c) 2500, (d) 5000, (e) 10000 cells per spheroid. (f)-(i) Comparison of Greenspan model simulated with maximum likelihood estimate (dashed lines) compared to synthetic data for first 6 days compared to Greenspan model simulated with known parameters used to generate the synthetic data (solid lines). Profile likelihoods for (j) $R_o(0)$, (k) s , (l) R_c , (m) γ , (n) Q . Yellow, orange, blue, and purple lines in (j)-(n) represent profile likelihoods from spheroids formed with 1250, 2500, 5000, and 10000 cells per spheroid, respectively. Black dashed lines in (j)-(n) show known parameters used to generate the synthetic data.

E.4 Increasing number of measurements

In biological experiments it is time consuming and expensive to increase the number of measurements obtained. However, by generating synthetic data we can easily simulate additional measurements. We generate 48 measurements of the outer radius, inhibited radius, and necrotic radius every half day from Day 0 to Day 20. We choose 48 measurements since this corresponds to half of a 96-well plate and is extremely large in comparison to typical experiments. These results show that many measurements of Design 2 may provide good insight in this extreme scenario but that Design 3 still provides most insight.

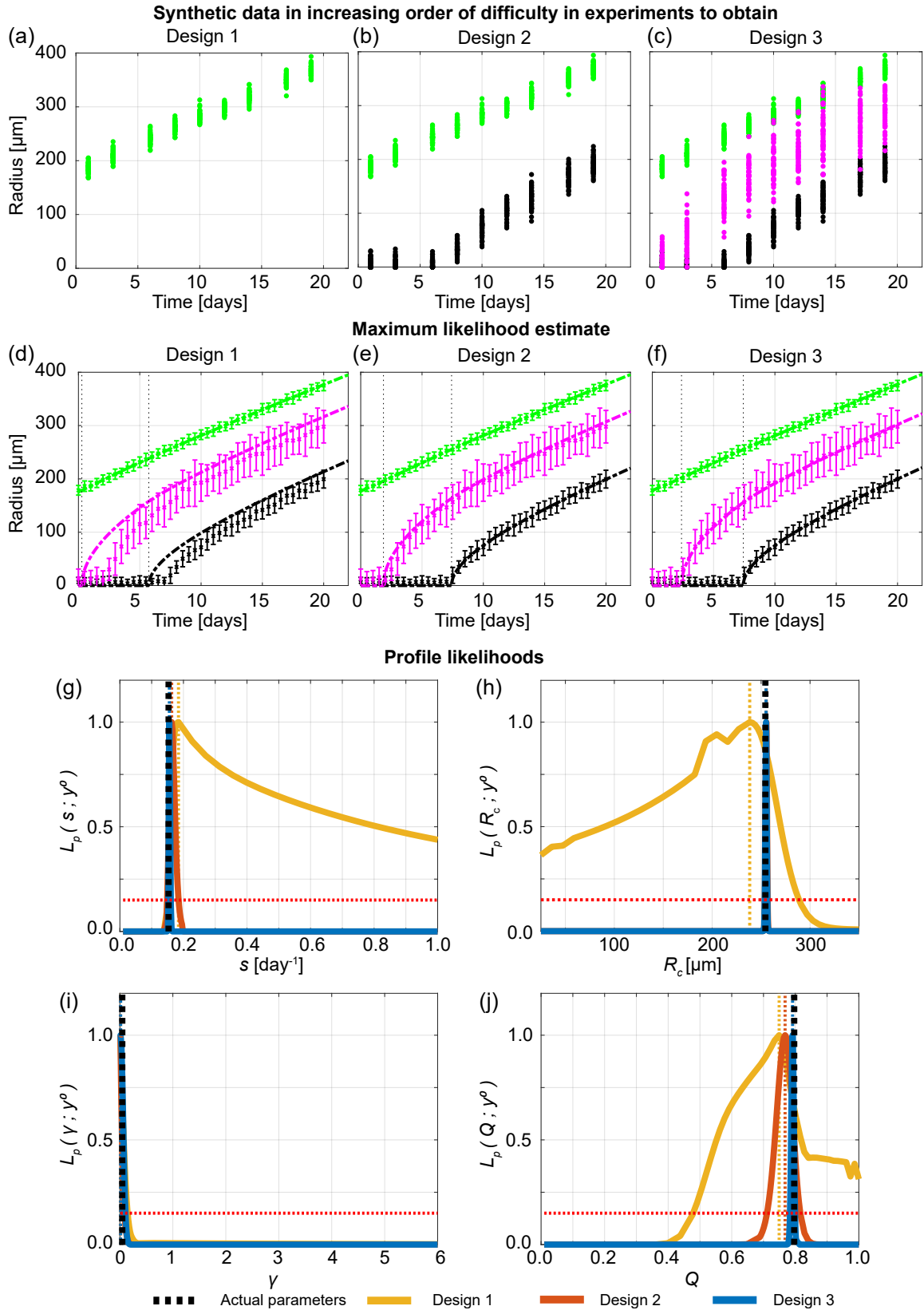


Figure S32: Synthetic data shows that more measurements of the necrotic and inhibited radius provide valuable information. (a)-(b) Synthetic data used in Designs 2 and 3. (c)-(d) Comparison of Greenspan model simulated with maximum likelihood estimate compared to full synthetic data set for Designs 2 and 3. Profile likelihoods for (e) s , (f) R_c , (g) γ , (h) Q . Yellow, orange, blue lines in (e)-(h) represent profile likelihoods from Designs 1 low temporal resolution, 2, and 3, respectively. Black dashed lines in (e)-(h) show known parameters used to generate the synthetic data.

F Parameter identifiability analysis for WM983b

The main manuscript focuses on results for the human melanoma WM793b cell line. Here, we present the corresponding results for the human melanoma WM983b spheroids formed with 2500, 5000, and 10000 cells.

All key observations made in reference to the WM793b cell line hold for the WM983b cell line. Specifically, in Figures S33, S34 and S35, for spheroids formed with 2500, 5000, and 10000 cells, respectively, we show that varying the temporal resolution using only Design 1 is insufficient to determine necrotic and inhibited radii. In Figures S36, S37, and S38 for spheroids formed with 2500, 5000, and 10000 cells, respectively, we show that Design 3 provides most insight. In Figure S39 we show that information gained across experiments with different initial spheroid sizes is consistent. Minor modifications were applied to the experimental designs as the WM983b cell lines form after 3 days, which is 1 day earlier than the WM793b, and the experiment was terminated after 19 days so the updated temporal resolutions are for this cell line are chosen as: Resolution A using Days 1, 3, 8, 12, 16; Resolution B using Days 1, 3, 5, 8, 10, 12, 14, 16, 18; Resolution C using Days 0, 1, 2, 3, 4, 5, 6, 7, 8, 9, 10, 11, 12, 13, 14, 15, 16, 17, 18; where Day 0 corresponds to the time that we determined as when spheroid formation ends and growth begins.

F.1 Outer radius measurements are not sufficient to predict inhibited and necrotic radii

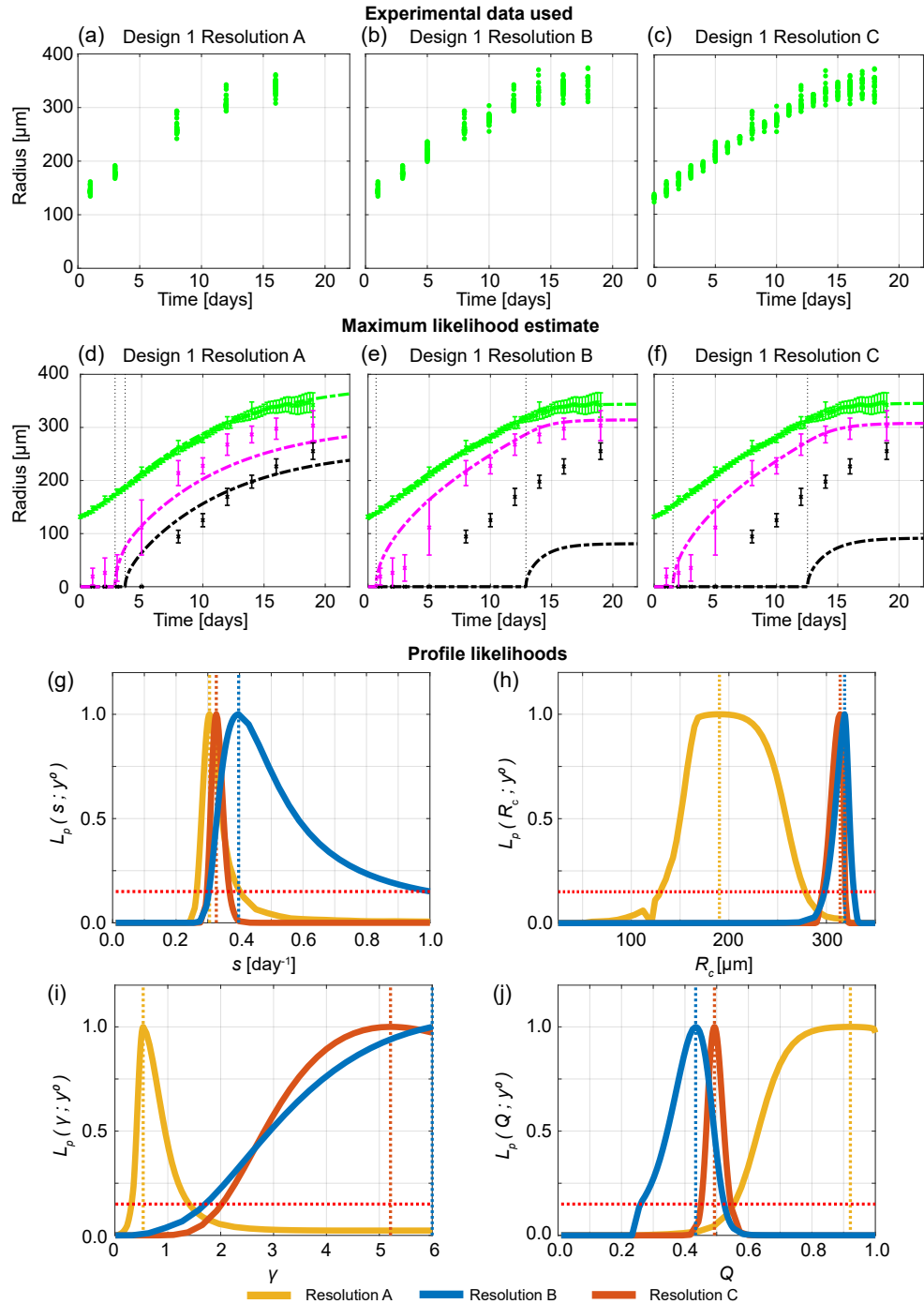


Figure S33: Increasing the temporal resolution when the outer radius is measured does not provide accurate information on internal structure. (a)-(c) Experimental data used in Design 1 with temporal resolutions A, B, and C. (d)-(f) Comparison of Greenspan model simulated with maximum likelihood estimate compared to full experimental data set, where error bars show standard deviation. Profile likelihoods for (g) s , (h) R_c , (i) γ , (j) Q . Yellow, blue, orange lines in (g)-(j) represent profile likelihoods from Design 1 with temporal resolutions A, B, and C, respectively, and the red-dashed line shows the approximate 95% confidence interval threshold. Results shown for WM983b spheroids formed with 2500 cells per spheroid.

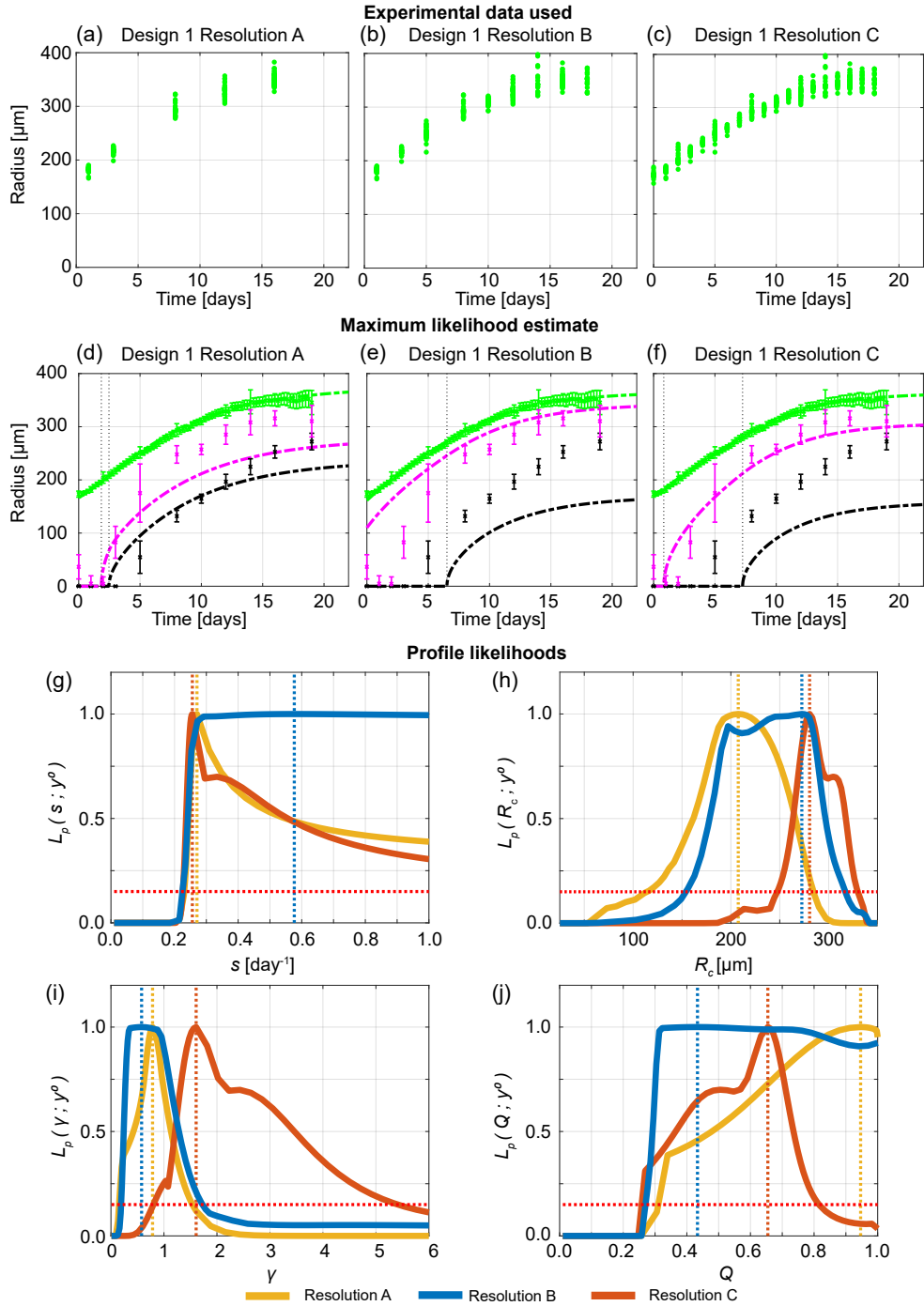


Figure S34: Increasing the temporal resolution when the outer radius is measured does not provide accurate information on internal structure. (a)-(c) Experimental data used in Design 1 with temporal resolutions A, B, and C. (d)-(f) Comparison of Greenspan model simulated with maximum likelihood estimate compared to full experimental data set, where error bars show standard deviation. Profile likelihoods for (g) s , (h) R_c , (i) γ , (j) Q . Yellow, blue, orange lines in (g)-(j) represent profile likelihoods from Design 1 with temporal resolutions A, B, and C, respectively, and the red-dashed line shows the approximate 95% confidence interval threshold. Results shown for WM983b spheroids formed with 5000 cells per spheroid.

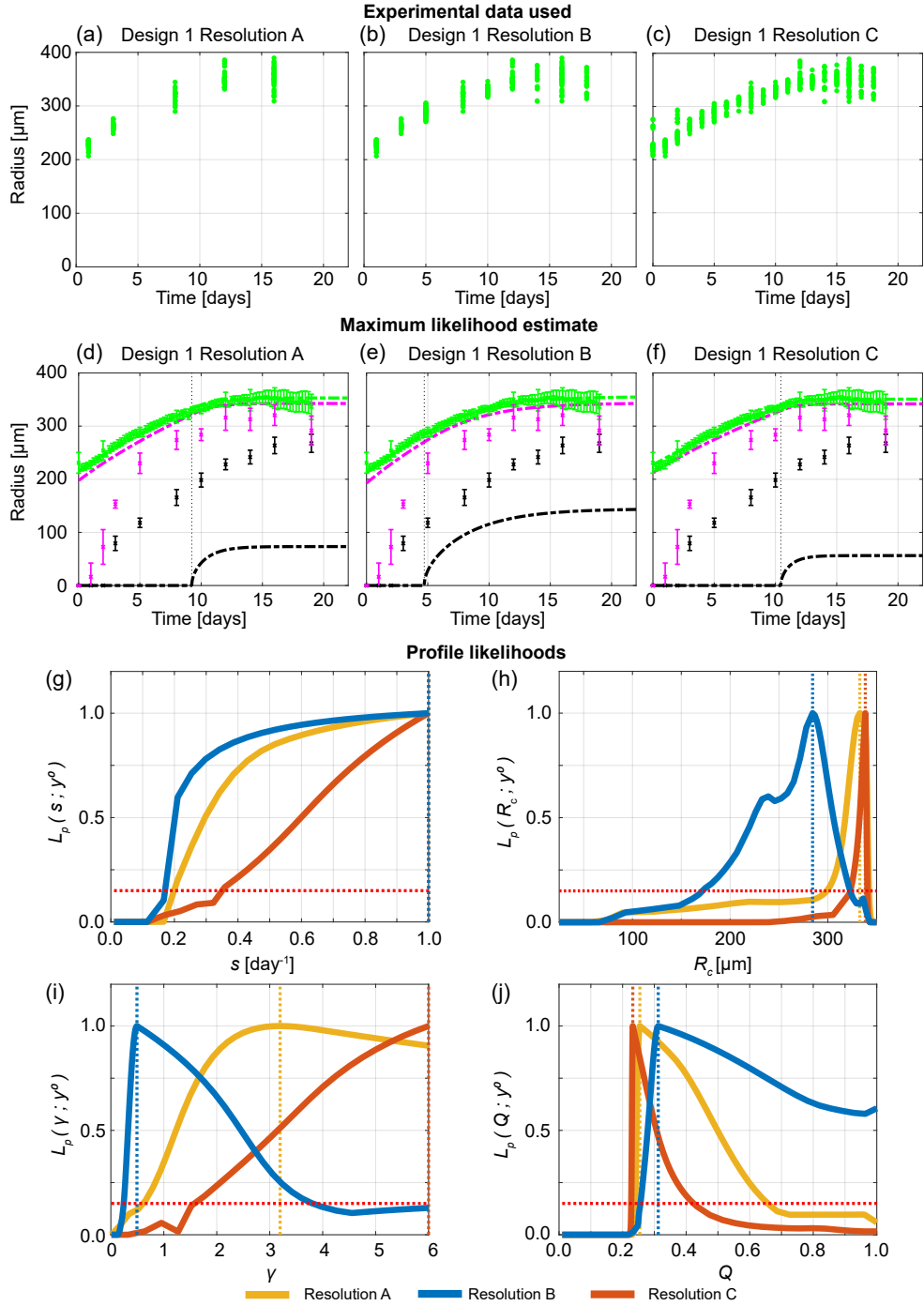


Figure S35: Increasing the temporal resolution when the outer radius is measured narrows approximate confidence intervals but does not provide accurate information on internal structure. (a)-(c) Experimental data used in Design 1 with temporal resolutions A, B, and C. (d)-(f) Comparison of Greenspan model simulated with maximum likelihood estimate compared to full experimental data set, where error bars show standard deviation. Profile likelihoods for (g) s , (h) R_c , (i) γ , (j) Q . Yellow, blue, orange lines in (g)-(j) represent profile likelihoods from Design 1 with temporal resolutions A, B, and C, respectively, and the red-dashed line shows the approximate 95% confidence interval threshold. Results shown for WM983b spheroids formed with 10000 cells per spheroid.

F.2 Cell cycle data are informative

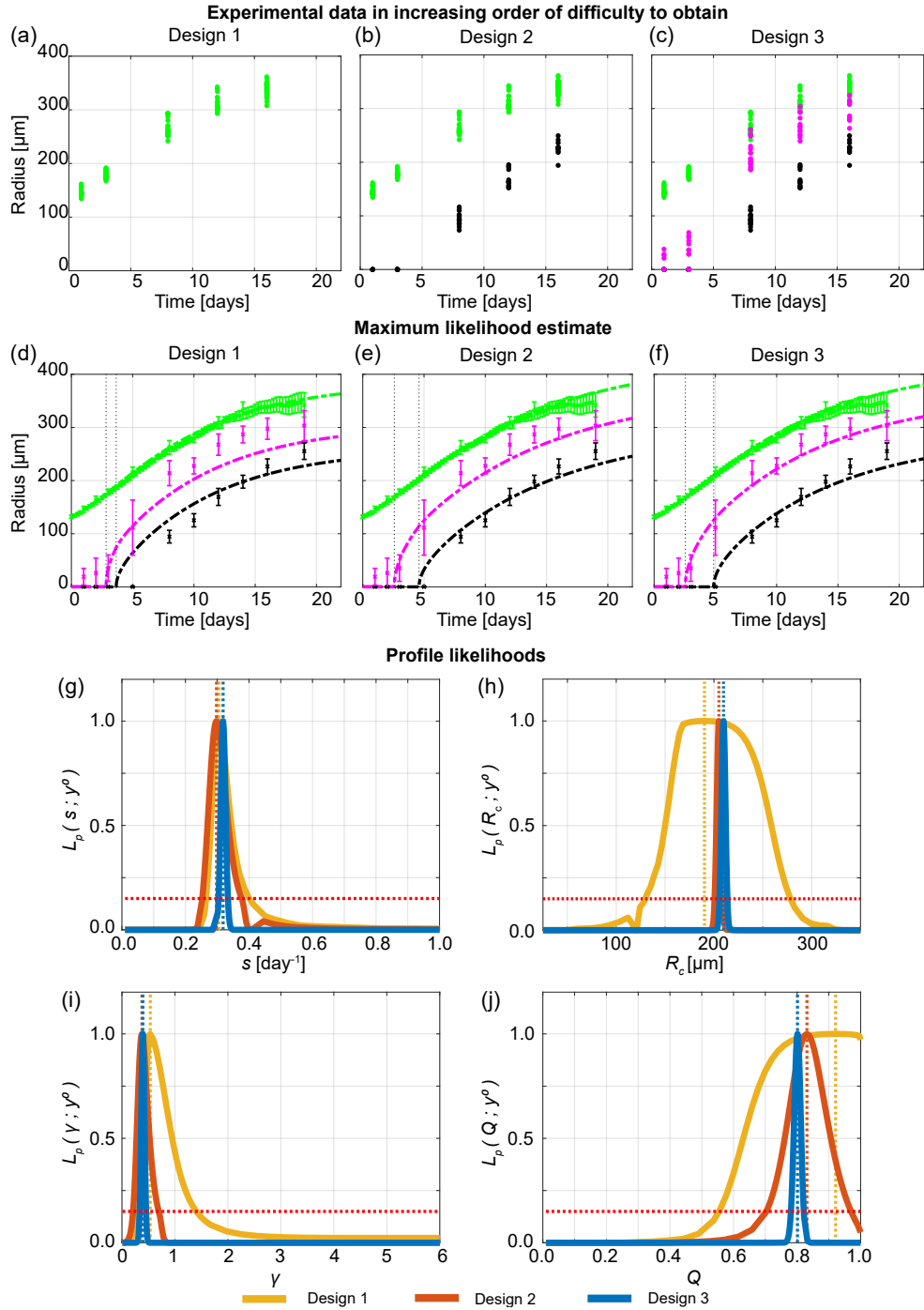


Figure S36: Measuring the necrotic and inhibited radius provides valuable information. (a)-(b) Experimental data used in Designs 2 and 3. (c)-(d) Comparison of Greenspan model simulated with maximum likelihood estimate compared to full experimental data set for Designs 2 and 3, where error bars show standard deviation. Profile likelihoods for (e) s , (f) R_c , (g) γ , (h) Q . Yellow, orange, blue lines in (e)-(h) represent profile likelihoods from Designs 1, 2, and 3, respectively, and the red-dashed line shows the approximate 95% confidence interval threshold. Results shown for WM983b spheroids formed with 2500 cells per spheroid.

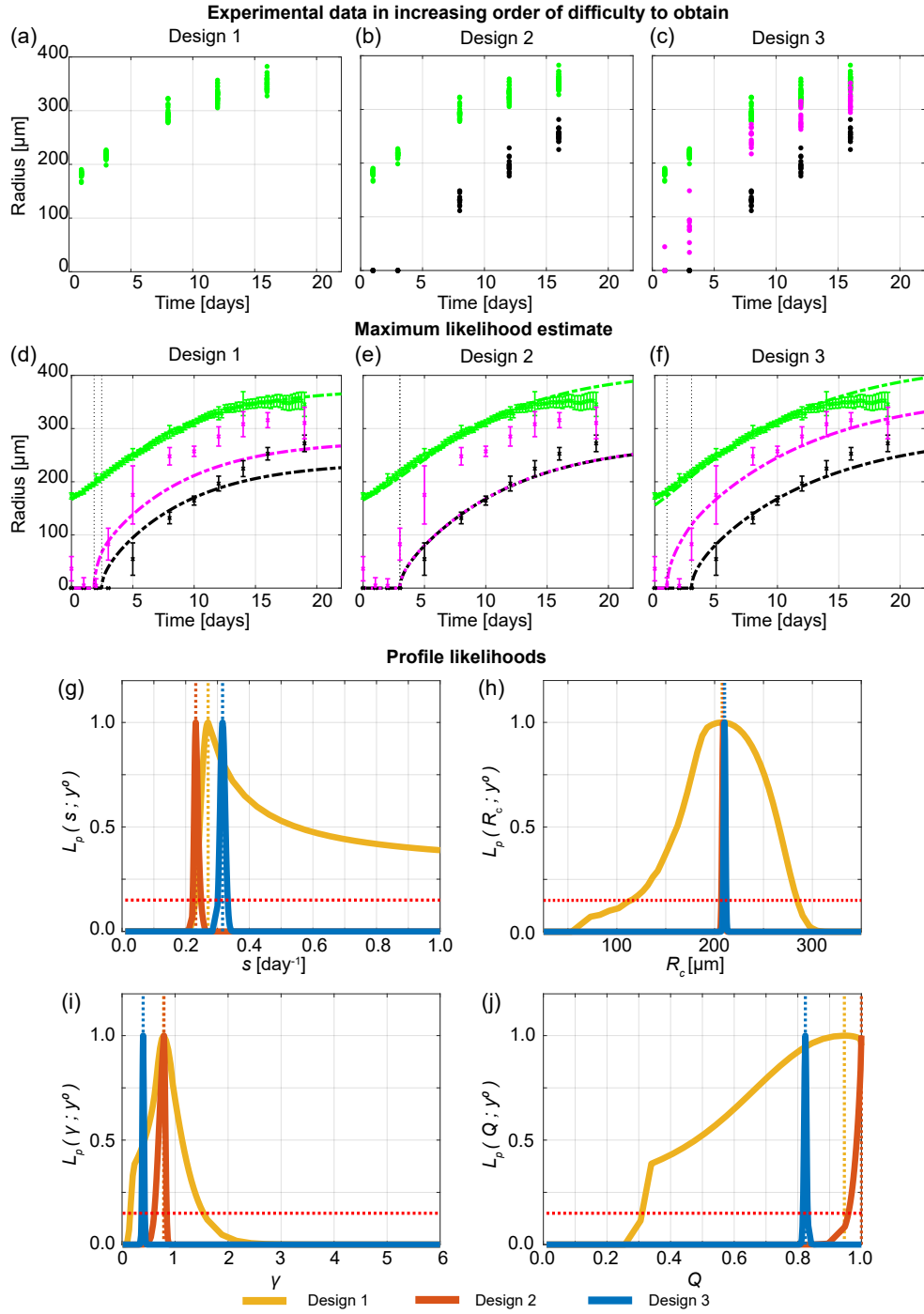


Figure S37: Measuring the necrotic and inhibited radius provides valuable information. (a)-(b) Experimental data used in Designs 2 and 3. (c)-(d) Comparison of Greenspan model simulated with maximum likelihood estimate compared to full experimental data set for Designs 2 and 3, where error bars show standard deviation. Profile likelihoods for (e) s , (f) R_c , (g) γ , (h) Q . Yellow, orange, blue lines in (e)-(h) represent profile likelihoods from Designs 1, 2, and 3, respectively, and the red-dashed line shows the approximate 95% confidence interval threshold. Results shown for WM983b spheroids formed with 5000 cells per spheroid.

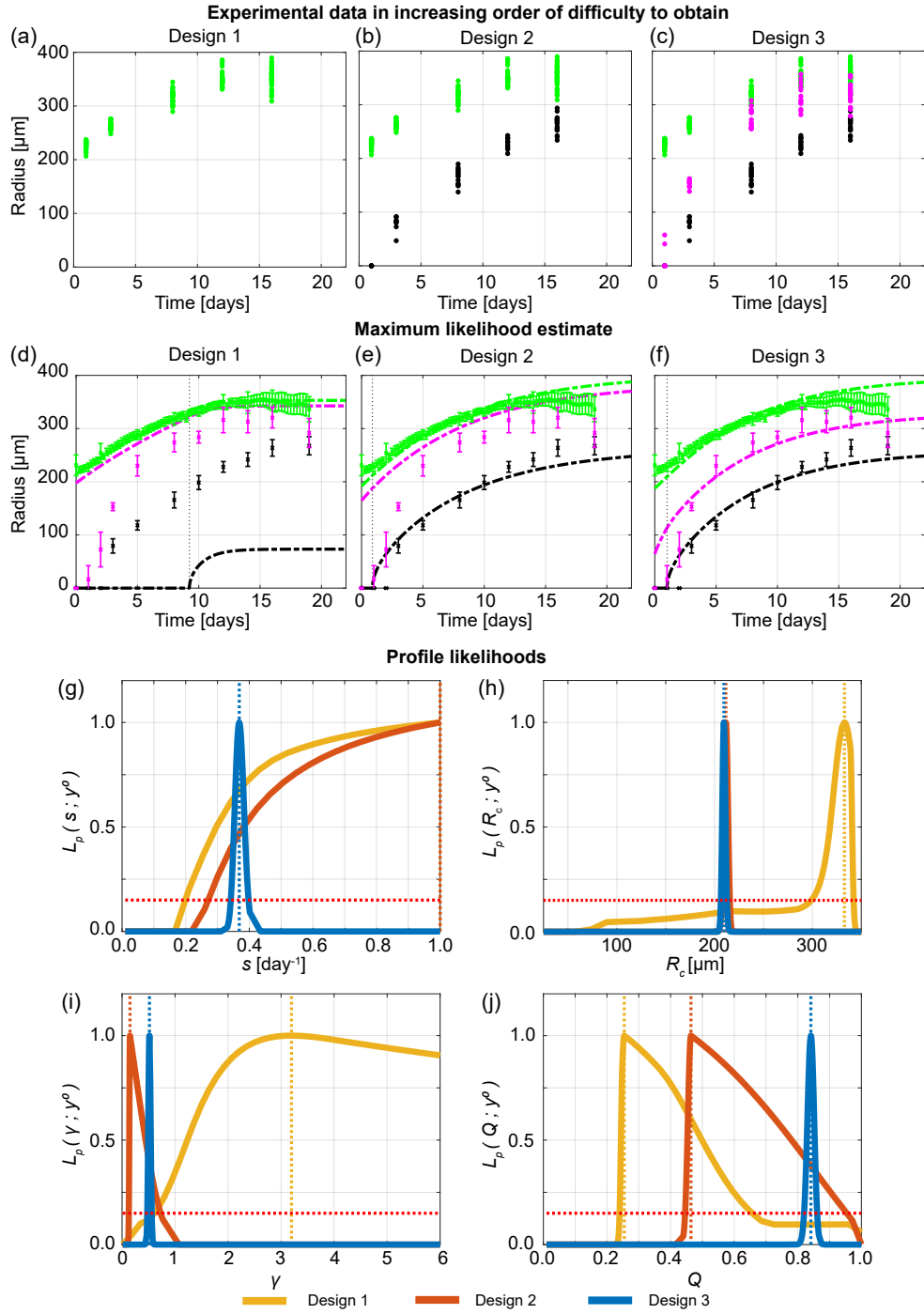


Figure S38: Measuring the necrotic and inhibited radius provides valuable information. (a)-(b) Experimental data used in Designs 2 and 3. (c)-(d) Comparison of Greenspan model simulated with maximum likelihood estimate compared to full experimental data set for Designs 2 and 3, where error bars show standard deviation. Profile likelihoods for (e) s , (f) R_c , (g) γ , (h) Q . Yellow, orange, blue lines in (e)-(h) represent profile likelihoods from Designs 1, 2, and 3, respectively, and the red-dashed line shows the approximate 95% confidence interval threshold. Results shown for WM983b spheroids formed with 10000 cells per spheroid.

F.3 Information gained across spheroid sizes is consistent

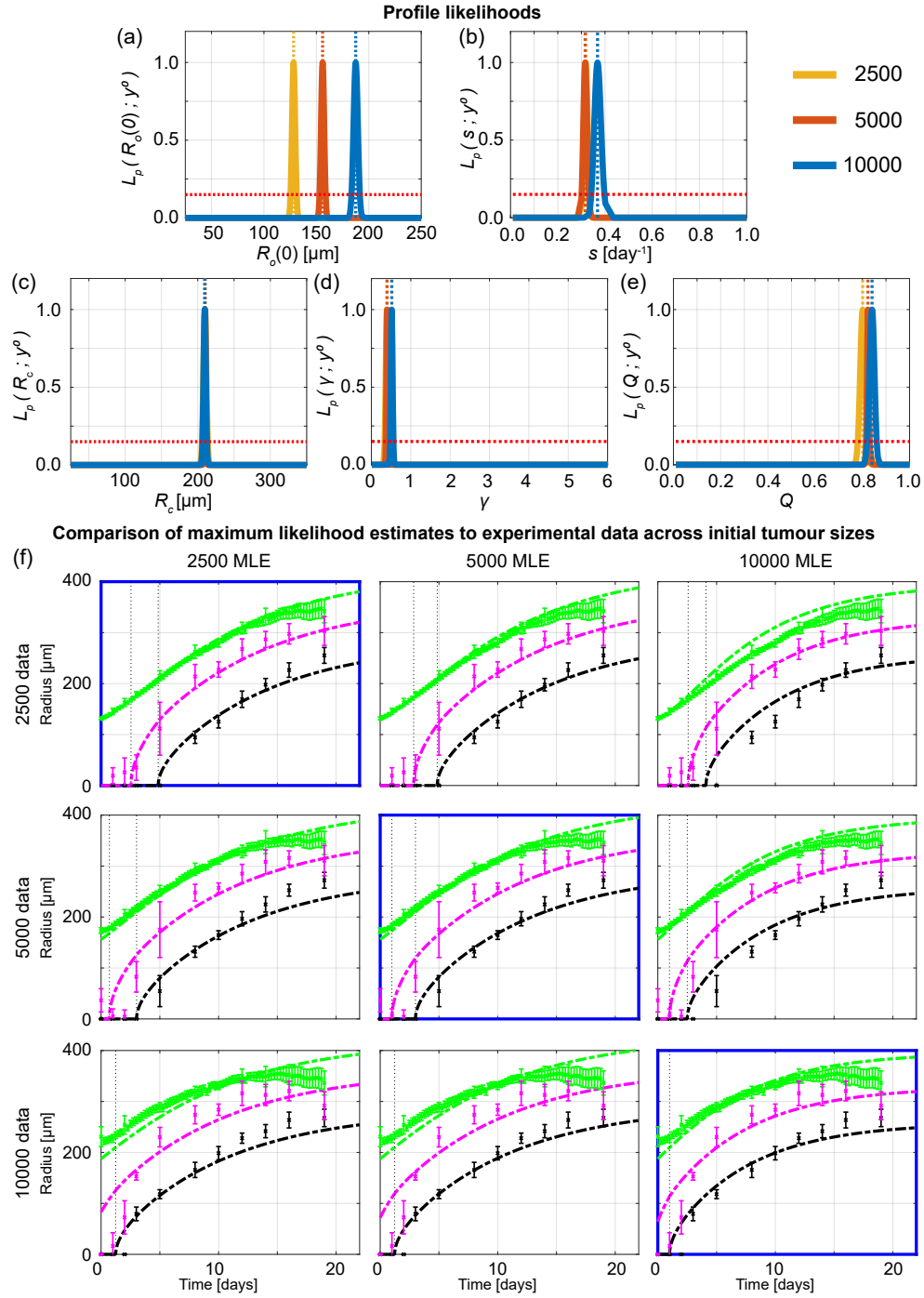


Figure S39: Information gained from experiments across different initial tumour spheroid sizes is mostly consistent. Profile likelihoods for (a) R_o , (b) s , (c) R_c , (d) γ , (e) Q . Yellow, orange, and blue lines in (a)-(e) represent profile likelihoods from tumour spheroids initially with approximately 2500, 5000, and 10000 cells per spheroid, respectively, and the red-dashed line shows the approximate 95% confidence interval threshold. (f) Comparison of Greenspan model simulated with maximum likelihood estimates compared to full experimental data sets across initial tumour spheroid size, where error bars show standard deviation. Results shown for WM983b cell line.

G Parameter identifiability analysis for WM164

The main manuscript focuses on results for the human melanoma WM793b cell line. Here, we present analogous results for the human melanoma WM164 spheroids formed with 1250, 2500, 5000, and 10000 cells per spheroid. These spheroids are more challenging to interpret as we will now explain.

In experiments WM164 spheroids formed after 3 days. These spheroids were larger in size than other spheroids considered in this work, with the initial radius of WM164 spheroids formed with 1250 cells per spheroid larger than and similar size to WM983b and W793b spheroids formed with 10000 cells per spheroid, respectively. The WM164 spheroids had relatively poor spherical symmetry [11], grew rapidly and many spheroids lost their structural integrity nine days after seeding formed with 1250, 2500, and 5000 cells per spheroid, and seven days after seeding for spheroids formed with 10000 cells spheroid. In addition, confocal microscopy could not be performed on day 7 after seeding for spheroids formed with 5000 and 10000 cells per spheroid due loss of structural integrity during harvesting. Identification of the necrotic region using image processing was more challenging, than for other cell lines, as a well-defined necrotic region did not form prior to the termination of the experiment. Therefore, necrotic region measurements for these spheroids are more subjective and uncertain. Spheroid boundaries were less smooth, so settings on the IncuCyte S3 live cell imaging system were updated to measure the largest brightfield object area with max eccentricity to 0.75 and sensitivity 20. These outer radius measurements were then manually reviewed to confirm accuracy.

We perform analysis for WM164 spheroids using Days 1, 2, 3, 4 and 5 after formation, where measurements could be obtained. This means that we do not include the last day of outer radius measurements for spheroids formed with 1250, 2500, and 5000 cells per spheroid. This allows us to compare the final outer radius measurement to Greenspan’s model simulated with the MLE as a predictive test. However, for spheroids formed with 10000 cells per spheroid we include all data points so cannot form a predictive test, but this is because we seek to obtain as much information as possible in the shorter experimental duration. While the experimental duration for WM164 spheroids is relatively short in comparison to the WM793b and WM983b experiments, these experiments are still performed for multiple days longer than previous WM164 spheroid experiments [12].

To perform the analysis we update initial parameter bounds, used for practical parameter identifiability analysis, for as $200 < R_o(0) < 600$ [μm] and $200 < R_c < 700$ [μm]. We update `FirstGuess` to $(Q, \gamma, s, R_c, R_o(0)) = (0.8, 0.1, 0.5, 400, 210)$ for spheroids formed with 1250 and 2500 cells per spheroid, and to $(Q, \gamma, s, R_c, R_o(0)) = (0.8, 0.1, 0.4, 400, 350)$ for spheroids formed with 5000 and 10000 cells per spheroid. Due to the reduced experimental duration for WM164 spheroids, and as we have already demonstrated with two other cell lines and synthetic data that Design 3 provides most insight, here we compare results obtained from spheroids with different initial sizes using Design 3.

In Figure S40a, we observe four distinct narrow peaks for $R_o(0)$ corresponding to the four initial spheroid sizes, which is expected. For s , we observe that profile likelihoods overlap showing information obtained for s is relatively consistent for different initial spheroid sizes (Figure S40b).

Interestingly and importantly, we observe four distinct peaks for R_c (Figure S40c). This lack of consistency is different to the other two cell lines considered and strongly suggests information gained across initial spheroid sizes is not consistent. This is supported by direct observation of the experimental data where spheroids formed with 2500 cells have necrotic cores on day 4, whereas similar sized spheroids on day 2 formed with 5000 and 10000 cells per spheroid do not. Profile likelihoods for γ are wide for spheroids formed with 5000 and 10000 cells per spheroid, and narrow and overlapping for spheroids formed with 1250 and 2500 cell per spheroid, showing that γ requires more necrotic core measurements to be identified (Figure S40d). Profile likelihoods for Q suggest that Q decreases as the initial spheroid size increases (Figure S40e). This result for Q is less consistent and in contrast to results from other cell lines, where the profiles for Q overlapped for all spheroid sizes. Overall, we conclude that, possibly due to their lack of spherical symmetry, WM164 spheroids are more challenging to interpret and information gained using spheroids of different sizes is not consistent.

To support these results, we show along the diagonal of Figure S40f the solution of the mathematical model evaluated at the MLE associated with each initial spheroid size compared to the experimental measurements. In doing so we demonstrate that we accurately predict the last outer radius measurement using previous days measurements for spheroids formed with 1250, 2500, and 5000 cells per spheroid. However, on the off-diagonals of Figure 4f, we compare how the Greenspan model simulated with the MLE from one initial spheroid size predicts data from different initial spheroid sizes by only changing the initial radius. These off-diagonal results show that using information from one spheroid size to predict the behaviour of a different spheroid size is not always accurate. For example, using information gained from spheroids formed with 10000 cell per spheroid poorly predicts the behaviour of spheroids formed with 1250 cell per spheroid, as the time evolution of the outer radius is not accurately predicted at late time and the inhibited and necrotic regions form much earlier than predicted (top right of Figure S40f).

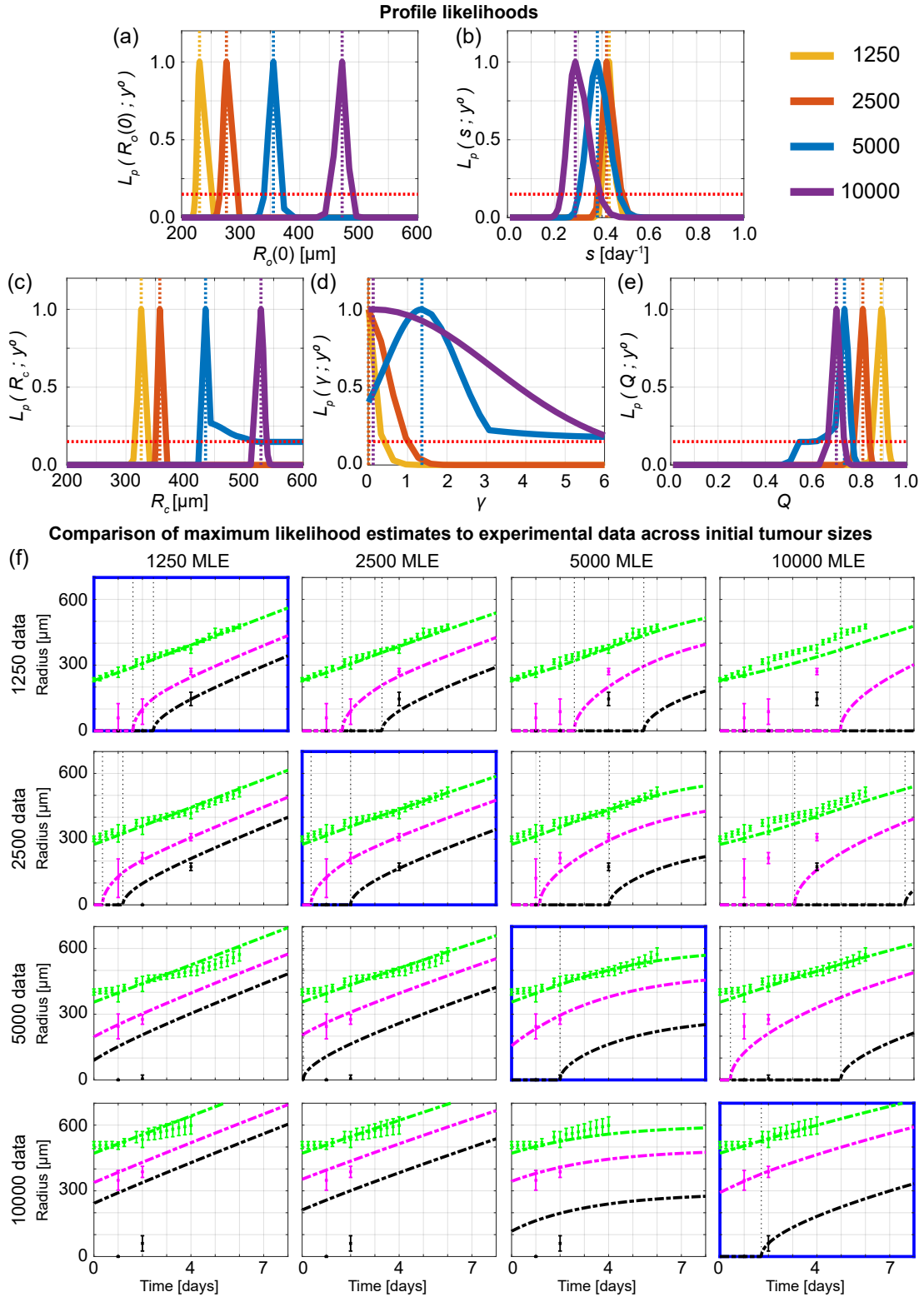


Figure S40: Information gained from WM164 experiments across different initial tumour spheroid sizes is inconsistent. Profile likelihoods for (a) $R_o(0)$, (b) s , (c) R_c , (d) γ , (e) Q . Yellow, orange, blue, and purple lines in (a)-(e) represent profile likelihoods from WM164 spheroids formed with 1250, 2500, 5000, 10000 cells per spheroid, respectively, and the red-dashed line shows the approximate 95% confidence interval threshold. (f) Comparison of Greenspan model simulated with maximum likelihood estimates compared to full experimental data sets across initial tumour spheroid size, where error bars show standard deviation.

References

- [1] MathWorks ode15s. <https://au.mathworks.com/help/matlab/ref/ode15s.html>. Accessed August 2021.
- [2] Murphy, K. C. *et al.* Measurement of oxygen tension within mesenchymal stem cell spheroids. *Journal of the Royal Society Interface* **14**, 20160851 (2017).
- [3] Grimes, D. R., Kelly, C., Bloch, K. & Partridge, M. A method for estimating the oxygen consumption rate in multicellular tumour spheroids. *Journal of the Royal Society Interface* **11**, 20131124 (2014).
- [4] Greenspan, H. P. Models for the growth of a solid tumor by diffusion. *Studies in Applied Mathematics* **51**, 317–340 (1972).
- [5] MathWorks normpdf. <https://au.mathworks.com/help/stats/normpdf.html>. Accessed August 2021.
- [6] Hines, K. E., Middendorf, T. R. & Aldrich, R. W. Determination of parameter identifiability in nonlinear biophysical models: a Bayesian approach. *The Journal of General Physiology* **143**, 401–416 (2014).
- [7] Warne, D. J., Baker, R. E. & Simpson, M. J. Using experimental data and information criteria to guide model selection for reaction–diffusion problems in mathematical biology. *Bulletin of Mathematical Biology* **81**, 1760–1804 (2019).
- [8] Browning, A. P., Haridas, P. & Simpson, M. J. A Bayesian sequential learning framework to parameterise continuum models of melanoma invasion into human skin. *Bulletin of Mathematical Biology* **81**, 676–698 (2019).
- [9] MATLAB Global Optimization Toolbox (2019). The MathWorks, Natick, MA, USA.
- [10] Pawitan, Y. *In all likelihood: statistical modelling and inference using likelihood* (Oxford University Press, Oxford, UK, 2001).
- [11] Spoerri, L. *et al.* Phenotypic melanoma heterogeneity is regulated through cell-matrix interaction-dependent changes in tumor microarchitecture. *Preprint on bioRxiv* (2021).
- [12] Haass, N. K. *et al.* Real-time cell cycle imaging during melanoma growth, invasion, and drug response. *Pigment Cell & Melanoma Research* **27**, 764–776 (2014).